Meteoric diffusion studies of middle atmospheric dynamical structure

A THESIS
SUBMITTED IN PARTIAL FULFILMENT
OF THE REQUIREMENTS FOR THE DEGREE
OF
MASTER OF SCIENCE IN PHYSICS
IN THE
UNIVERSITY OF CANTERBURY
by

Gareth Thomas

University of Canterbury
1998

Abstract

This work investigates the use of ambipolar diffusion coefficients determined by the decay times of meteors detected by the University of Canterbury's meteor radar, AMOR, in determining dynamical parameters for the middle atmosphere. The radar system has the ability to accurately determine the geometric altitude of detected meteor trains, thereby making it a potentially powerful tool for detailed and continuous observation of the atmosphere.

Software has been developed in the IDL interperative language to analyse the data in two main ways. Firstly a brief analysis of the relationship between geometric altitude and ambipolar diffusion coefficient was made. As with all previous work the logarithmic relationship predicted between the two was confirmed on average, although a very large degree of true scatter was found. The density scale height inferred by this analysis was found to be in reasonable agreement with recent previous results.

The major part of the analysis done used the ambipolar diffusion coefficient as a measure of temperature change and investigated these changes over time. Three time scales were investigated; variations over a few hours, daily behaviour and long term change over months and years. All three scales showed evidence of time dependent structure. The short time scale analysis showed evidence of fluctuations consistent with gravity wave propagation. Mid time scales showed a diurnal oscillation, but the source of this is unclear. Long time scales showed an annual variation in agreement with the broad temperature structure of the middle atmosphere.

Acknowledgements

I would like to thank my supervisor, Prof. Jack Baggaley, for his assistance and guidance throughout this project and Dr. Bryan Lawrence for also providing much assistance with the atmospheric dynamics and computing aspects.

Finally my thank you to the rest of the atmospheric group, particularly Steve Marsh and David Galligan, for their advice and company.

Contents

Figures

Chapter 1

Introduction

1.1 Basic Picture

The space through which the Earth moves in it's orbit about the Sun is not empty, in fact the Earth's path is crossed by countless small particles also orbiting the Sun. These particles, know as *meteoroids*, range from micrometers to a few meters in size, with the great majority being at the small end of the scale. Obviously, with so many meteoroids in the Earth's vicinity many enter the atmosphere. It is the effects of these collisions and their use in investigating the middle atmosphere which are the concerns of this project.

When a meteoroid travelling at many kms^{-1} encounters the Earth's atmosphere friction causes extreme heating and the particle reaches a temperature of about 2000 K. This temperature is enough to cause vaporisation of the surface of the meteor, and the collisional energies between meteor and atmospheric particles is high enough to cause ionisation. Hence, as a meteoroid passes through the upper atmosphere it creates a trail of glowing plasma (called an *ionisation train*), and for meteoroids greater than about 5 mm in diameter it is this we see as a "shooting star" or *visual meteor*. Most meteoroids are small enough to be completely vaporised in the passage though the atmosphere, but the occasional larger one has enough mass for fragments to reach the ground as *meteorites*.

Despite the fact that very small meteors are not easily observed visually they can still be detected using a suitable radar system. This is because the ionisation train left by a meteor contains a large enough concentration of free electrons to act as a good reflector of radio waves. Meteors detected in this fashion are known as *radio meteors*. This project uses data collected using such a system operated by the University of Canterbury's Physics Department, AMOR[1].

The meteoroids themselves originate mostly from comets. As a comet approaches the sun from the outer reaches of the Solar System the increased Solar radiation causes evaporation and out-gassing, which in turn releases a large amount of dust. Because of the initial dispersion in velocity of ejected material a tube-like trail of meteoroids is created following the comet's orbit, and when the Earth passes through such a trail a *meteor shower* results. From the ground a meteor shower can be seen as a period of intense activity, with all the meteors appearing to come from the same point in the sky (a perspective effect due to the parallel paths of the particles), this point is called the radiant of the shower. Over time the particles in these tubes have their orbits perturbed by the gravitational effects of the planets

[1] the Advanced Meteor Orbit Radar

and it is these perturbed meteoroids which cause the much more common *sporadic meteors*. Other sources of sporadic meteors include debris from collisions between larger bodies in the Solar System (most notably asteroids) and even interstellar material [1].

1.2 Project organisation and purpose

This project is an investigation into the suitability of the AMOR system for measuring dynamical processes (namely wavelike structures) near the mesopause by the calculation of the ambipolar diffusion coefficients of meteor trains.

The rest of this chapter gives an overview of meteor and atmospheric science. Chapter 2 presents the theory of meteor detection by radar and gives the theoretical basis for two possible uses for ambipolar diffusion data for the atmosphere. Chapter 3 Describes the AMOR system, the data acquisition and storage and the practical determination of ambipolar diffusion coefficients from meteors. Chapter 4 examines the relationship between the geometric altitude of a meteor trail and it's measured diffusion coefficient. Chapter 5 presents the results of searches for wavelike structures in the AMOR diffusion data and compares these with previous and/or expected results.

1.3 Historical overview

The observations of and attempts to explain meteors go back thousands of years, but it was only in the 1790's that a truly scientific attempt was made to determine their origin and nature. The astronomer Chladni was the man who inadvertently caused this development when he put forward a theory in 1794 that space is filled with particles that ignite when they encounter the Earth's atmosphere. This idea inspired a couple of German students, Brandes and Bezenberg, to carry out simultaneous observations of meteors in 1798 while separated by several kilometres. By simple triangulation they were able to determine that the meteors were occurring at a height of some 100 km, and that the velocities of the particles creating them were planetary in magnitude. This rather inspired work was however a flash in the pan, as interest in meteors remained low until the spectacular Leonid meteor shower of 1833 stirred up immense public interest. This sparked off a rush of visual meteor observing geared towards determining meteor rates and the radiant positions of showers. This work continued for about the next 100 years, providing little of importance as far as actual atmospheric science went. The main development in the 19th century was the realization that many meteor showers had very similar orbits to known comets, thereby offering an explanation to their origin.

Virtually all knowledge of conditions in the middle and upper atmosphere has been gained in this century, and it was observations of meteors that provided some of the early data on the region. In 1923 Lindemann and Dobson [2] used visual meteor observations to derive a density profile for the atmosphere for the region from 60 to 160 km. They used two stations, each with trained observers simul-

taneously recording the path, direction and (very roughly) speed of any meteors seen. Using this information and triangulation between the stations they were able to determine the height of appearance and disappearance (where the ionisation train becomes visible and where the meteor is completely vaporised respectively). This in turn was used to estimate the density of the atmosphere at these heights. The profile they derived from this was considerably different from that expected, suggesting a temperature of about 300 K - much higher than should exist in a non-absorbing atmosphere at such heights. The solution to this discrepancy was put down to the heat developed by the reactions of ozone.

Other techniques latter re-enforced and improved on the findings of Lindemann and Dobson. For instance in 1929 Bendorf [3] suggested that the zones of silence and then audibility of heavy gunfire noticed during the First World War at very large ranges ($\sim$ 200 km) could be explained by an increasing temperature with height in the region we now call the stratosphere. In 1936 Martyn and Pulley [4] published a temperature of the atmosphere using a wide range of measurements from many researchers. Spectroscopy of the Aurora [5], their own radio studies of the E-region of the ionosphere, observations of noctilucent clouds at about 82 km, the propagation of sound from explosions and audible meteors [6] and work on the ozone layer [7] were all used. The temperature profile gained from these methods is very close to what is accepted today, with a temperature maximum at about 60 km (although Martyn and Pulley's value of 450 K at this altitude is now known to be a gross over estimate), a temperature minimum of 160 K near 80 km and an increasing temperature with altitude above this.

It wasn't until the development of photographic meteor observation that the parameters necessary for both Solar System orbital and atmospheric information to be extracted from meteor observation could be calculated with any accuracy. The 'standard' system for photographic meteor observation was first developed by Elkin at Yale in 1893. He used two cameras, separated by 3.3 or 5.0 km but pointing at the same area of sky, with rotating shutters (made from bicycle wheels) in front of the lenses. The rotating shutter would cause an image of a meteor to be segmented, the spacing of the segments giving the angular velocity of the meteor, and this in combination with triangulation using the two sites enabled a complete solution of the path parameters. Unfortunately the spacing of his cameras was not great enough to be effective.

This method has been used by numerous researchers, and indeed is still in use, but the most extensive program of this type can be attributed to Whipple [8] in the late 1930's. Whipple was involved in the Harvard photographic patrol program, which was initially set up to take routine time exposures of the sky to provide a long term record for specific astronomical purposes such as detecting variable stars and determining the orbits of minor planets. Meteors had long been recorded on the Harvard plates and to maximise the information available from this unexpected source Whipple made modifications that basically made the system analogous to Elkin's, except with a 38 km base line. The main emphasis of visual meteor observation has been geared towards getting orbital parameters for the meteoroids detected, but Whipple also used the Harvard data to derive a temperature profile

of the upper atmosphere in 1943 [9]. Using the height of maximum brightness, the heights of detection and disappearance and the deceleration of the meteor he developed an atmospheric profile with a maximum temperature of 375 K at 62 km and a value of 250 K near 80 km.

Meteor photography has also provided information on upper atmospheric winds. By the way they deform, long enduring meteor trails can give indications of the wind conditions in the meteor region.

Although visual techniques have provided valuable information on meteors they suffer from several draw backs. They are confined to the hours of darkness and periods of good weather; photographic images are very difficult to analyse electronically and digitally stored images (which are good for computer analysis) tend to require a lot of storage space. These problems are solved by the use of a radar to observe meteors, and hence it is with radar that the bulk of recent progress has been made in the area. The first meteors detected by radar were in the late 1920's, appearing as fluctuations in echoes received from the E-region. It was Skellet, in 1931, who first showed that a meteor could cause a sudden increase in ionisation needed to explain such fluctuations. In the same year his suggestion was verified when Schafer and Goodall used simultaneous visual and radio observations of the Leonid Meteor shower.

During World War II great advances were made in radar technology due to it's usefulness in providing long range detection of aircraft. After the war this technology was soon modified for use in meteor detection. Indeed, the radar network used by the British Army for directing anti-aircraft gun fire was kept operational for a few months after hostilities ended particularly to investigate in more detail the echoes from meteors it had been detecting during the war.

In using meteors to measure upper atmospheric parameters by radar two broad techniques are applied. Continuous wave radar compares the transmitted frequency to that of an echo, thereby giving a Doppler Shift. The radial velocity given by this Doppler Shift represents the wind velocity, in the radial direction, at the location of the specular reflection point on the meteor trail. By pulsing the radar, range can be determined (by timing the lag between transmitting a pulse and receiving it's echo), and by estimating the height a picture of the wind conditions in the meteor zone can be gained. Because these radars can operate 24 hours a day and produce large amounts of data they provide an opportunity to continuously monitor the winds at around 100 km. An example of early work in this area is that done by Greenhow and Newfield in the mid 1950's at Jodrell Bank in Britain [10, 11]. A system like this (although with more accurate altitude determination) is also operational for use with the AMOR radar of Canterbury [12].

The other main type of radar used is a incoherent pulse radar. This technique uses the return time of the pulse to give the range and records the echoes amplitude with time. If multiple receiving stations are used meteor velocities can be calculated (by using the time differences between the occurrence of specular reflection at different sites) and interferometry can give the elevation of an echo. It is a system like this that has provided the data for this project and a more complete description of the capabilities of such a radar will be given in Chapter 3 where the AMOR system

will be described.

The other major development since World War II for studying the upper atmosphere has been the development of rocketry. This has enabled much more direct measurements of the upper atmosphere. Rockets have been used to carry measuring instruments into the upper atmosphere as well as releasing vapour trails or objects to be studied from the ground. Techniques include:

- Pressure sensors to determine atmospheric density.
- Dropping objects of known frictional coefficient and then tracking their decent with radar (again to determine density profiles).
- Creating explosions at predetermined height intervals and recording the sound at different locations on the ground (the propagation of sound can again give information on atmospheric density).
- Observation of the effect of wind shear and turbulence on the vapour trail left by a rocket.
- Spectral analysis of the vapour trail light, giving temperature information and when taken with the diffusion rate, density.
- Mass spectrometers have even been carried, enabling direct measurements of the upper atmospheric composition to be made.

Although rockets provide a huge source of reliable information, they are expensive and only give a snap-shot of the atmosphere at a given time. They are therefore most useful as a check and calibration on other observation programs.

The other thing that rocketry has given upper atmospheric science is the artificial satellite (such as the Upper Atmosphere Research Satellite, UARS [2]) which enable continuous measurements covering large portions of the globe to be performed. Of course satellites suffer from the cost problem as well, and they tend not to provide detailed long term data sets for a given region.

1.4 The atmosphere

Figure (1.1) shows the basic temperature structure of the Earth's atmosphere as well as the adopted nomenclature. As can be seen the atmosphere can be divided into four broad temperature regions. The lowest of these is the troposphere (0 to $\sim$ 12 km), the region we are all familiar with. The temperature falls with altitude at roughly the adiabatic lapse rate (although this is altered by the presence of large amounts of water vapour). Because the temperature gradient is in the same direction as the density gradient the atmosphere is vertically unstable — hence the atmospheric composition is very uniform in this region. Chemistry plays a very

[2]The UARS Project Document is available on the world wide web at http://daac.gsfc.nasa.gov/CAMPAIGN_DOCS/UARS_project.html

minor roll in controlling the temperature in the troposphere, dynamics and Solar heating of the Earth's surface are the controlling factors.

Next comes the stratosphere, so called because the positive temperature gradient with height produces a stable, stratified structure. The major cause of this reversal of temperature gradient is the photochemical reactions of ozone. As we move up through the stratosphere the absorption of solar U.V. radiation by O_2 increases (as the flux of U.V. radiation left to be absorbed increases). This solar absorption produces the well know Chapman cycle of ozone production and loss;

$$\begin{array}{lcll} O_2 + h\nu & \rightarrow & O^* + O^* & (\text{meta} - \text{stabel excitation}) \\ N_2 + O^* & \rightarrow & N_2 + O & (N_2 \text{ heated}) \\ O + O_2 & \rightarrow & O_3^* & \\ O_3^* + N_2 & \rightarrow & O_3 + N_2 & (N_2 \text{ heated}) \\ O_3 + h\nu & \rightarrow & O_2 + O & \\ O + O_3 & \rightarrow & 2O_2 & \end{array} \tag{1.1}$$

This cycle (as well as the many other reactions and processes which occur) are sufficient to raise the temperature from about 200 K at the tropopause to around 300 K at the stratopause (at about 50 km).

In the mesosphere the rapidly falling atmospheric density reduces the amount of heating from photo-chemistry, and the temperature again falls. In this region ionising solar radiation begins to play a more prominent role in the chemistry, and thereby the thermal conditions. At about 80 km the heating primarily from the dissociation of O_2 is great enough to cause the temperature to begin rising again after reaching a minimum of roughly 200 K. The temperature continues to increase through the thermosphere until atmospheric particles become indistinguishable from solar wind particles. Hence the conditions in the upper atmosphere are extremely dependent on the level of solar activity, the temperature at 500 km ranges between 500 K and 1800 K.

Throughout the atmosphere the pressure and density drop approximately exponentially — both being solely determined (to first approximations) by the mass of atmosphere above the point in question. The composition of the atmosphere is however more complicated. At low altitudes the atmosphere is almost entirely composed of neutral species, the main constituents being N_2 ($\sim$ 80% by volume) and O_2 ($\sim$ 20%) with CO_2, H_2O and other gases in trace amounts. This continues to be the basic mix up to about 100 km, apart from the increase in the abundance of O from the stratosphere upwards. Below 100 km the density of all species decreases with altitude at the same rate (neglecting changes due to chemistry) as the time taken for gases to reach diffusive equilibrium is longer than the vertical mixing time, even in the relatively stable stratosphere. This region of the atmosphere is known as the *homosphere*. Above 100 km however diffusive equilibrium is reached and each species decreases in density according to it's own scale height. The result of this is that the abundance of the lighter consitutence drops off much less rapidly than in the homosphere (where the density drops at a rate basically determined by N_2). Also at about 100 km the abundance of O becomes greater than that of O_2 and, due to the low mass of O compared to N_2, O becomes the most common

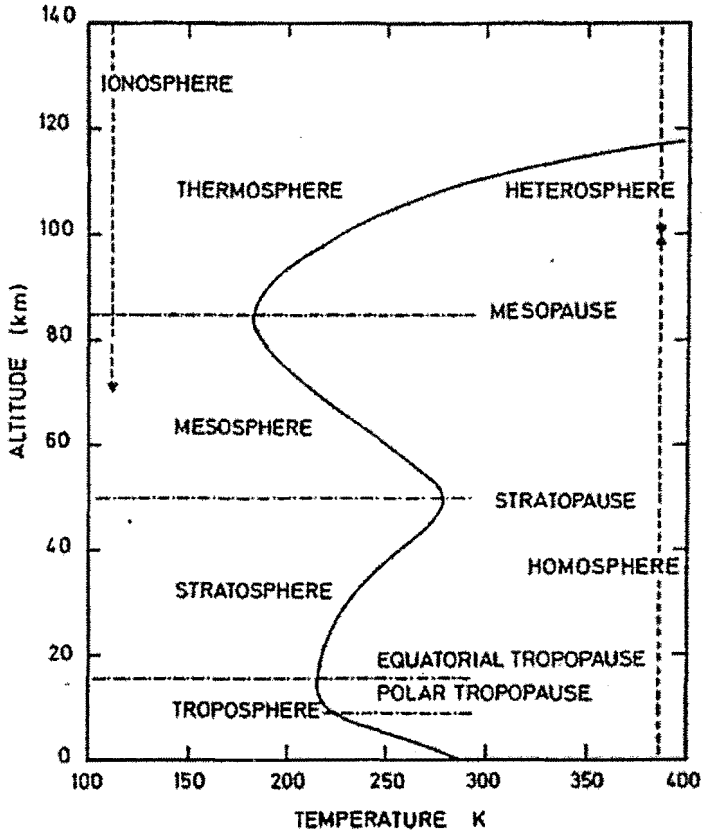

Figure 1.1: The approximate temperature structure and layers of the Earth's atmosphere [After Brassear and Solomon [13]].

species above about 300 km. O_2 rapidly decreases in abundance to become only a minor constituent by the time He becomes dominant at around 600 km. Finally, at around 1000 km atomic H becomes dominant.

As already mentioned, high in the atmosphere Solar radiation causes ionisation. As with ozone production ionisation occurs in relatively narrow vertical regions, for the same reasons as mentioned for ozone creation. There are four main regions of ionisation called, in ascending order, the D, E, F_1 and F_2 regions.

The D region is caused by the ionisation of NO by Lyman α radiation (there being a "window" in the ionisation curve of O_2 at the Lyman α band). The peak of the D region is at around 80 km and it is only present during daylight (loss processes remove the ionisation rapidly in the absence of sunlight).

The E region is generated by the ionisation of O_2. It was the first of the ionisation layers to be discovered, reflecting radio waves in the E band. The peak ionisation occurs at about 100km and, as with the D region, the layer is absent at night.

The F_1 and F_2 regions are both due to the ionisation of N_2 and O. The F region is dived into two "subregions" because of the ionisation loss processes active at different altitudes. N_2^+ is lost rapidly through radiative recombination at all levels, but the recombination of O^+ is more complicated and depends strongly on altitude. Because radiative recombination of O^+ is extremely slow the ionisation is lost through a charge exchange process. In the F_1 region (which peaks at around 150 km) the atmospheric density is high enough to allow charge exchange reactions between O^+ and either O_2 and N_2 to take place very rapidly. This provides an efficient loss mechanism for O^+, since the recombination reactions of the O_2^+ and NO^+ products of the charge exchange reactions are also rapid. Above about 200 km however the abundances of O_2 and N_2 become low enough that the charge exchange reactions become slower than the recombination reactions. The charge exchange reactions rapidly become extremely slow and the ionisation levels increase again to form a second peak at about 400 km. Due to the very long ionisation loss time in the F_2 region it is the only layer to remain during the night.

Throughout the ionosphere the atmosphere is only a very weak plasma. The strongest relative ionisation occurs at the peak of the F_2 region where the ratio of free electrons to neutral atmospheric particles is about 1:100.

1.4.1 Dynamics

What is referred to as the meteor zone in this thesis is the altitude region approximately bounded by 80 and 110 km, i.e. the region surrounding the mesopause. This area of the atmosphere is of great interest as it marks transition in more than temperature. As can be seen in figure (1.1) the meteor zone girdles not only the mesopause but also the start of the ionosphere and the transition to the hetrosphere. Of more importance to this project is that the mesopause also marks a transition in the dynamics of the atmosphere.

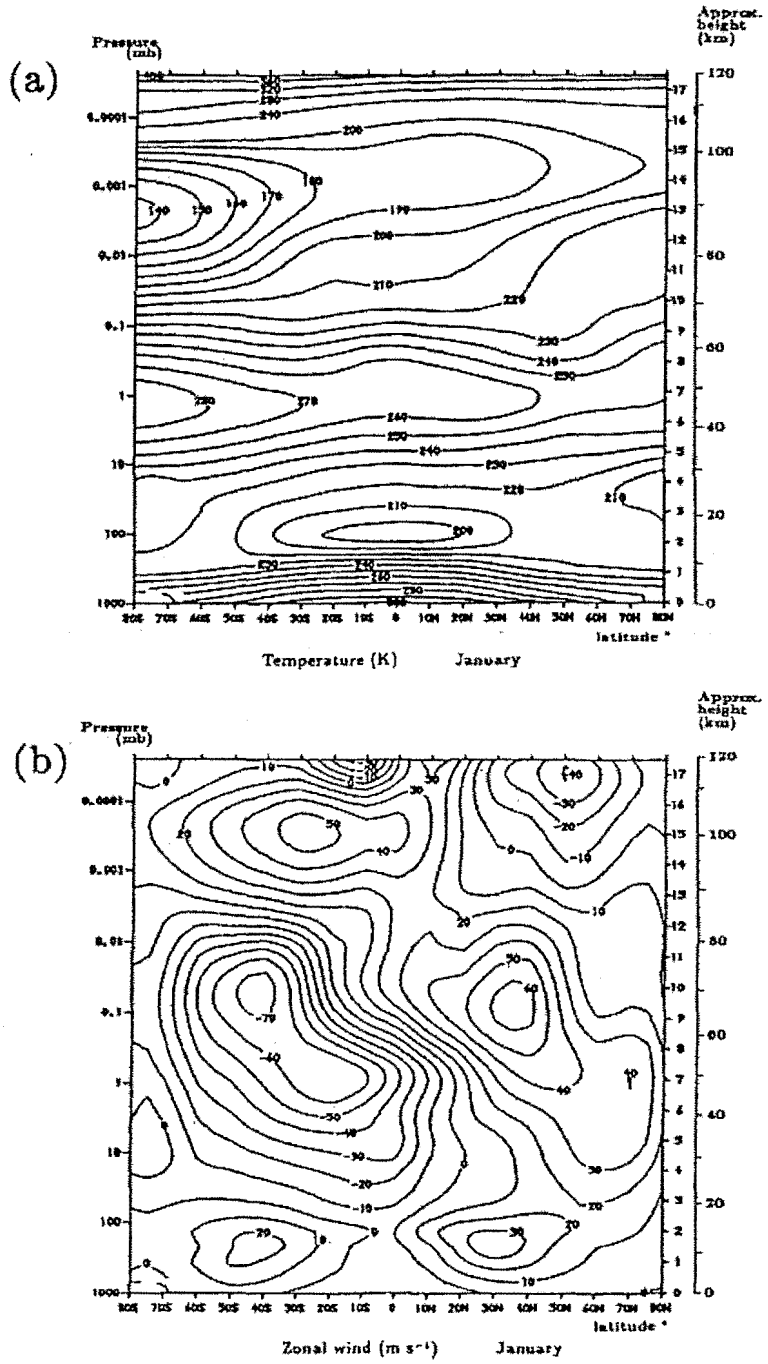

Figure 1.2: The monthly zonal mean latitude vs. pressure scale height (first right ordinate, running from 0 to 17) for (a) temperature and (b) zonal wind (with eastward motion labelled as positive) in January from CIRA-86 [After Brassuer and Solomon [13]].

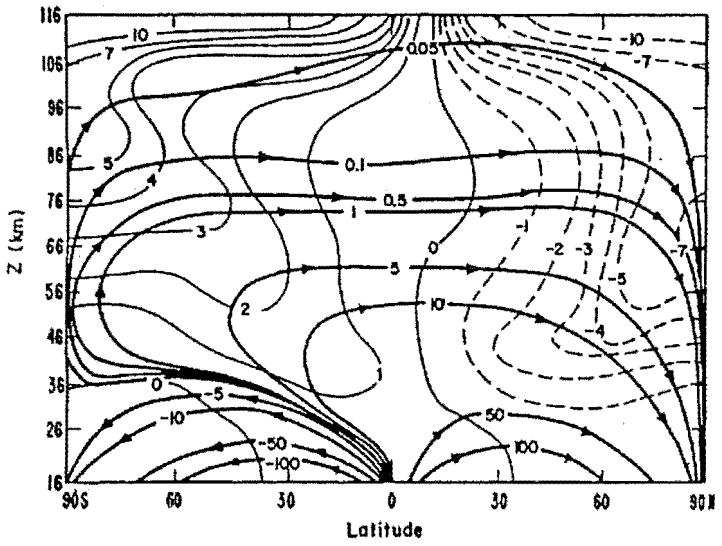

Figure 1.3: A two-dimensional model prediction mass stream function for the meridional circulation (heavy dark lines, $\mathrm{kg\,m^{-1}s^{-1}}$ and diabatic heating distribution (light solid and dashed lines, $\mathrm{K\ day^{-1}}$) for southern hemisphere summer [After Garcia and Solomon [14]].

The dynamics and temperature structure of the lower atmosphere can be considered, on a broad scale the product of latitudinal and seasonal differences in solar heating. Air near the equator is heated, rises and moves to higher cooler latitudes where it sinks again. Air from the higher latitudes is itself drawn towards the equator at low altitudes to replace the air rising above the equator. The action of the Coriolis force on these flows of air moving toward the poles produces the eastward jets seen in figure (1.2b) below about 20 km and is responsible for the westerly motion of weather systems in the troposphere. As can be seen in figure (1.3) the upward convection near the equator is strong enough to extend this circulation into the lower stratosphere, thereby providing a mechanism for tropospheric air to enter the vertically stable stratosphere. The effect of such circulation can also be seen in figure (1.2a), where adiabatic cooling results in a temperature minimum over the equator in the lower stratosphere. This description does not describe the complex meteorological processes at work in the troposphere only the broad average motion and temperature profile. To account the complex system we experience as weather we must include the interactions of the atmosphere with the topographic and temperature variations of the Earth's surface.

In the mesosphere however figure (1.3) shows a different situation. Here the flow is from the summer to winter poles and is driven by the deposition of momentum in the mesosphere by (principally) upward-propagating gravity waves. Once again the effect of this flow can be seen in the zonal flow between 20 and 90 km (figure (1.2b)), the Coriolis force producing westward and eastward jets in the summer and winter hemispheres respectively. The temperature profile in this region is more dominated by photochemistry with ozone heating providing a temperature maximum over the summer pole.

Above the mesopause the characteristics change once again. We now find a temperature minimum over the summer pole, caused by adiabatic cooling of the air rising to become part of the flow towards the winter pole (figure (1.3)). There is also a reversal in the direction of the zonal winds, with an eastward jet now being found in the summer hemisphere and a westward jet found in the winter hemisphere. Above 70 km the exact mechanisms controlling the general circulation are less understood. Parallels have been draw between the dynamics found near the mesopause and the large scale weather systems found in the troposphere [15, 16]. It is known that the general circulation is driven by dynamics, with meridional circulation being driven by vertical momentum flux produced by planetary waves, tides, gravity wave and turbulence (as with the mid-mesosphere), but the relative importance of these processes in controlling the general circulation is not yet known. There is a need for more data on the processes producing momentum fluxes near the mesopause to allow this problem to be addressed. It is hoped that data from the AMOR system can detect and allow the measurement of wavelike structures of a broad range of scales near the mesopause and provide one such window on the dynamics controlling this region. Without an understanding of the dynamical processes controlling the circulation in the upper atmosphere modelling the lower regions becomes difficult — the atmosphere cannot be treated as a stack of isolated regions.

Chapter 2

Model of radar echoes

2.1 Diffusion coefficients of meteor trails by radar

There are two broad types of meteor echoes detected by radar, the classification depending on the electron density within the train at formation. If the electron line density q is higher than about $2.4 \times 10^{14}\mathrm{m}^{-1}$ then the echo is said to be *overdense* - the radio waves do not penetrate the trail but are effectively reflected from it's surface. (This picture is a simplification as the ionisation decreases as the distance away from the trains axis increases, hence the radio waves do penetrate the column to some degree. However as far as the echo received is concerned this model is completely adequate). An overdense meteor echo is characterised by a rapid rise to a maximum echo amplitude as the train forms, followed by a period of fairly constant amplitude (neglecting the effects of wind) followed by a exponential decay as electron density drops below $2.4 \times 10^{14}\mathrm{m}^{-1}$ due to diffusion. Wind can drastically alter this picture however, causing the train to distort and thereby producing large amplitude changes in the echo due to interference from multiple reflection points.

If q is low the echo is termed *underdense* - the radiation penetrates the trail and each electron acts an individual scattering source (ignoring secondary radiative and absorptive effects, a good approximation in the rarefied atmosphere near the mesopause). The transition between the two is, of course, gradual. This project uses the decay times of underdense trains to calculate the diffusion coefficient for the atmosphere, so we will concentrate on the physics of the underdense meteor train.

Underdense meteor echoes are characterised by a rapid increase to maximum amplitude level, followed immediately by an exponential decay, often with Fresnel diffraction oscillations (a geometric effect) superimposed on the decay. Figure (2.1) shows the geometry of a meteor train. We assume that the train is made up of stationary electrons and the diameter of the train is much smaller than the wavelength of the radar.

The scattering cross-section of a free electron is $\sigma_e = \pi r_e^2 \sin^2\gamma$ where r_e is the classical radius of the electron and γ is the scattering angle. For backscatter $\gamma = \pi/2$, implying $\sigma_e \approx 1 \times 10^{-28}$ m^2. The power flux incident on the train is $\Phi_i = P_T G_T / 4\pi R^2$ where P_T is the transmitted power, G_T is the antenna gain in that direction relative to an isotropic radiator and R is the range to the train. The effective absorbing area of the receiving antenna is $G_R \lambda / 4\pi$, where G_R is the gain of the receiver relative to an isotropic radiator. Thus the power appearing at the

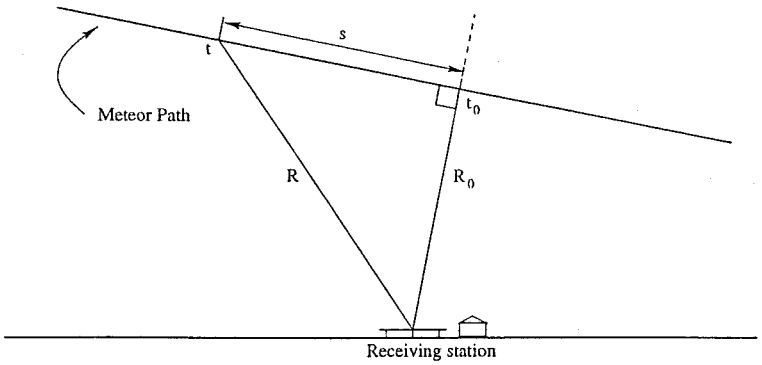

Figure 2.1: The geometry of a meteor train relative to a radar receiver.

input of the receiver due to the backscattered signal from one electron is

$$P_e(R) = \frac{P_T G}{4\pi R^2} \frac{\sigma_e}{4\pi R^2} \frac{G\lambda^2}{4\pi} = \frac{P_T G_T G_R \lambda^2 \sigma_e}{64\pi^3 R^4} \tag{2.1}$$

As all the electrons in a line element, ds, will scatter in phase (assuming the width of the trail at formation is much smaller than λ) the field vectors, rather than the power fluxes must be added. At the receiver the peak amplitude of the field due to a single scattering electron is $(2rP_e)^{\frac{1}{2}}$, where r is the receiver input impedance. The absolute phase of the returning wave, which has covered a distance $2R$, is included in the time varying expression $\sin(2\pi ft - 4\pi R/\lambda)$, in other words the change in R produces a modulation in the phase of the returning wave. Now we may write an expression for the instantaneous amplitude of the received signal from all the electrons in the line element ds.

$$\mathrm{d}A_R = (2rP_e)^{\frac{1}{2}} q(t) \sin\left(2\pi ft - \frac{4\pi R}{\lambda}\right) \mathrm{d}s \tag{2.2}$$

where $q(t)$ is the number of electrons per meter path (electron line density).

By integrating we can now write an expression for the total field due to the electrons in the trail between s_1 and s. For simplicity we take $q(t)$ as being constant along the train and use the approximation $R \approx R_0 + s^2/2R_0$. We also make the transformations $\chi = 2\pi ft - 4\pi R_0/\lambda$ and $2s = x(R_0\lambda)^{\frac{1}{2}}$, giving

$$A_R = \frac{(2rP_eR_0\lambda)^{\frac{1}{2}}}{2} q(t) \int_{x_1}^{x} \sin\left(\chi - \frac{\pi x^2}{2}\right) \mathrm{d}x \tag{2.3}$$

The Fresnel integrals of optical diffraction theory are

$$\mathcal{C} = \int_x^{x_1} \cos\left(\frac{\pi x^2}{2}\right) \mathrm{d}x \quad \text{and} \quad \mathcal{S} = \int_x^{x_1} \sin\left(\frac{\pi x^2}{2}\right) \mathrm{d}x$$

Substituting these into equation (2.3) gives

$$A_R = \frac{(2rP_eR_0\lambda)^{\frac{1}{2}}}{2} q(t) \left[\mathcal{C} \sin\chi - \mathcal{S} \cos\chi\right]. \tag{2.4}$$

Because the maximum oscillation frequency of the Fresnel integrals is much less than the radio frequency f we can take a time-average over an interval which is small compared to the smallest oscillation period of $\mathcal{C}$ and $\mathcal{S}$. This gives an expression for the quasi-instantaneous power P_R received from the electrons in the trail between s and s_1

$$P_R = \frac{A_R^2}{2r} = \frac{P_e R_0 \lambda}{2} \left[\frac{\mathcal{C}^2 + \mathcal{S}^2}{2}\right] q^2(t) \tag{2.5}$$

which, on substituting equation (2.1) and parameters in SI units, yields (in units of watts)

$$P_R = 2.5 \times 10^{-32} P_T G_T G_R \left(\frac{\lambda}{R_0}\right)^3 \left[\frac{\mathcal{C}^2 + \mathcal{S}^2}{2}\right] q^2(t) \tag{2.6}$$

This is the basic expression giving the echo power from an underdense train and it has exactly the form as that describing the optical diffraction pattern produced from a Fresnel straight edge optical experiment (neglecting any time dependence of q).

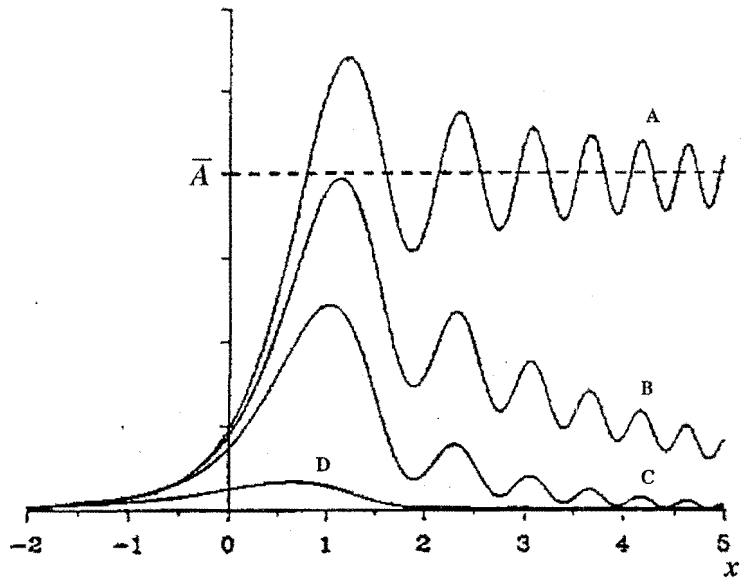

Figure 2.2: Examples of the functional form of equation (2.6) without the affect of diffusion (curve A), and with increasing levels of diffusion (curves B,C and C). Curve A clearly shows the rapid rise to maximum followed by Fresnel oscillation about the mean amplitude $\bar{A}$.

The term

$$\left[\frac{\mathcal{C}^2 + \mathcal{S}^2}{2}\right]$$

has the value of unity when evaluated from $s = -\infty$ to $+\infty$. Although our approximation of R doesn't allow us to move very far from the t_0 (specular reflection)

point, this term is close to unity when taken over a few Fresnel zones either side of t_0. In other words, the more remote sections of the train do not contribute noticeably to the echo power.

We now have an expression that describes the echo received from a ionisation train as it is being formed, but we have yet to include any mechanism for reducing the electron density in the train and thereby causing the echo to decay. To do this we assume that the train, once formed extends infinitely in both directions from the specular reflection point and that is not affected by wind shear or turbulence. The second of these assumptions is untrue in most cases, but it greatly simplifies the following analysis.

A meteor train, once formed, is a column of plasma made up of several different ion species, and in isolation these would all diffuse at a different rate. However this tendency is counteracted by the electronic attraction between the different ions and the free electrons, the plasma diffuses at one rate. This is known as *ambipolar diffusion* and it is the most important factor governing the reduction of echo power after the train has formed, reducing the volume density without affecting the line density. There have been many treatments of ambipolar diffusion of meteor trails (see [17, 18]). The method is to set up and solve differential equations describing radial diffusion of a cylindrical distribution of electrons and positive ions, usually neglecting magnetic effects.

The radial distribution of density we will use is a Gaussian, although this is simply a mathematical convenience as it has been shown that the initial density distribution has no effect on the diffusion rate of the train [19]. The standard form of the radial diffusion equation is

$$\frac{\partial N}{\partial t} = \frac{D}{r}\frac{\partial}{\partial r}\left(r\frac{\partial N}{\partial r}\right) \tag{2.7}$$

where N is the volume density of electrons at time t and distance r from the axis and D is the ambipolar diffusion coefficient in $\mathrm{m^2 s^{-1}}$. We take one solution of equation (2.7)

$$N = \frac{1}{A(t+k)} e^{[-r^2/B(t+k)]} \tag{2.8}$$

where A, B, and k are all constants. Substitution into equation (2.7) shows that $B = 4D$. A is found by applying the condition that the total number of electrons in an infinite cross sectional slice of unit thickness must be equal to q at all times. If we take a annular ring of radius r we find that it contains $2\pi r N dr = \pi N d(r^2)$ electrons, and so we can say

$$q = \int_0^\infty \frac{\pi}{A(t+k)} e^{[-r^2/4D(t+k)]}\, \mathrm{d}(r^2) = \frac{4\pi D}{A} \tag{2.9}$$

So the volume density can be expressed as

$$N(r,t) = \frac{q}{\pi(4Dt + r_0^2)} e^{[-r^2/4Dt + r_0^2]} \tag{2.10}$$

where we have replaced the term $4Dk$ with r_0^2, the square of the trail's initial radius.

Since we are now discussing the change in echo amplitude due to the radial diffusion of a meteor trail we must take the radial distribution of electrons into account as there will be interference effects as the effective radius of the train changes [20]. Although calculating the amplitude of the scattered signal in this way is a 3-dimensional problem, a good approximation can be obtained by simply considering the phase effects near the specular reflection point, where the echo is strongest.

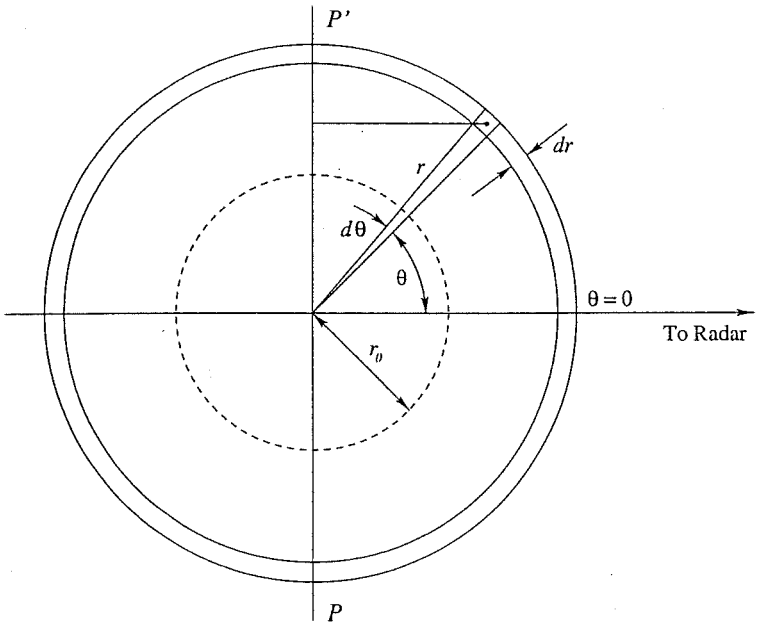

Figure 2.3: Cross section of an underdense trail near the t_0 point, showing the coordinate geometry used.

If we take an annular ring of radius r and radial width $\mathrm{d}r$ (figure (2.1)), centered about the center of the train and perpendicular to it's axis, the electron density will be constant throughout the ring. The amplitude of the backscattered signal from all the electrons within the ring will be

$$\mathrm{d}A = 2Nr\ \mathrm{d}r \int_0^{\pi} \sin\left(2\pi f t - \frac{4\pi r}{\lambda}\cos\theta\right) \mathrm{d}\theta \tag{2.11}$$

where the phase angle $(4\pi r/\lambda)\cos\theta$ of the electrons in the element $r\ \mathrm{d}r\ \mathrm{d}\theta$ is with respect to a plane of zero phase, PP', perpendicular to the line of sight to the radar. Expanding this integral using trigonometric identities we get

$$\mathrm{d}A = 2Nr\ \mathrm{d}r \left[\sin 2\pi f t \int_0^{\pi} \cos\left(\frac{4\pi r}{\lambda}\cos\theta\right)\ \mathrm{d}\theta\ +\ \cos 2\pi f t \int_0^{\pi} \sin\left(\frac{4\pi r}{\lambda}\cos\theta\right)\ \mathrm{d}\theta\right] \tag{2.12}$$

and since

$$\int_0^{\pi} \cos\left(\frac{4\pi r}{\lambda}\cos\theta\right) \mathrm{d}\theta = \pi J_0\left(\frac{4\pi r}{\lambda}\right) \tag{2.13}$$

and the integral involving the sine function is zero we have

$$\mathrm{d}A = 2\pi N J_0 \left(\frac{4\pi r}{\lambda}\right) r\ dr\ \sin 2\pi f t \tag{2.14}$$

This amplitude will always be less than that obtained if all electrons are taken to lie along the trail axis, but the phase will be the same. Hence if we integrate along the trail and take the ratio of the total scattered amplitude and the total amplitude obtained from a trail with infinitesimal width we obtain

$$\frac{A}{A_0} = \frac{2\pi \int_0^\infty N J_0(4\pi r/\lambda) r\ \mathrm{d}r}{2\pi \int_0^\infty N r\ \mathrm{d}r} \tag{2.15}$$

Substituting the value of N from equation (2.10) into equation (2.15) we then integrate. The denominator is simply q, the numerator is non-trivial however (see [21]). The result of this is

$$\frac{P_R(t)}{P_R(t_0)} = \left(\frac{A}{A_0}\right)^2 = e^{[-32\pi^2 Dt/\lambda^2]} e^{[-8\pi^2 r_0^2/\lambda^2]} \tag{2.16}$$

where $P_R(t_0)$ is given by equation (2.6). Equation (2.16) shows that the received power is immediately cut by a factor of $\exp[-8\pi^2 r_0^2/\lambda^2]$ due to the finite initial width of the trail, and then continues to decrease exponentially due to a time dependent diffusion factor. The *decay time constant* τ is defined as the time taken for the amplitude to decay by a factor of e^{-1}, so from equation (2.16) we have

$$\tau = \frac{\lambda^2}{16\pi^2 D} \tag{2.17}$$

This is an important result as it says that the ambipolar diffusion coefficient of an underdense meteor train is inversely proportional to the decay time constant of a radar echo from that train, with the only other parameter being dependent only on the radar system employed. As discussed in section (2.2), the diffusion constant is in turn an indicator of temperature and density conditions in the section of atmosphere that the meteor occurred in. For further information on the theory of meteor radar echoes see [22].

2.2 The dependence of diffusion coefficient on atmospheric parameters

2.2.1 Diffusion rate as a measure of altitude

It can been shown that, neglecting electron-ion collisions, the ambipolar diffusion coefficient can be expressed as $D \approx D_i(1+\frac{T_e}{T_i})$ where D_i is the positive ion diffusion coefficient, T_i is the ion temperature and T_e is the electron temperature [18]. The time taken for the ion and electron temperatures to reach the neutral temperature has been shown to be small [23] so

$$D \approx 2D_i. \tag{2.18}$$

In turn D_i is given by

$$\begin{aligned} D_i &= K_i(kT/e) \\ &= \frac{8}{3\pi n\sigma_i^2}\sqrt{\frac{kT}{\pi\mu}} \end{aligned} \tag{2.19}$$

where K_i is the ionic mobility. Here k is Boltzmann's constant, T the atmospheric temperature, e the electronic charge, n the atmospheric number density, σ_i the average collisional diameter for ions with air molecules and μ is the mean ionic mass (assumed to be equal to the mean air molecule mass). It is obvious then that the dependence of the diffusion coefficient on atmospheric parameters is not a simple one at all, and we have not considered the influence of other factors such as the Earth's magnetic field.[1] There have been, therefore, been many attempts to apply simplifications to this relationship in the hope of gaining useful information from diffusion data.

As early meteor radar systems were very limited in their ability to measure the altitude of an echo, the diffusion rate was initially used as a measure of the trail height. If an isothermal atmosphere is assumed then $n \propto p$, the atmospheric pressure. As a function of altitude p is given by

$$p = p_0 \exp\left(\frac{h_0 - h}{H}\right) \tag{2.20}$$

where

$$H = \frac{kT}{mg} \tag{2.21}$$

is the atmospheric scale height, h_0 is the altitude at which the pressure is p_0 and h is the height. As can be seen from equation (2.19) $D \propto 1/n$ in an isothermal atmosphere with uniform composition. Therefore we can substitute D for pressure in equation (2.21) giving

$$1/D = 1/D_0 \exp\left(\frac{h_0 - h}{H}\right) \tag{2.22}$$

If we take logarithms of both sides we find a linear relationship between altitude h and $\ln D$ with a slope equal to the scale height,

$$\frac{\mathrm{d}h}{\mathrm{d}\ln D} = H. \tag{2.23}$$

Greenhow and Neufeld [25] performed one of the early investigations into this relationship. On average they found good agreement between their theoretical predictions and observed echo decay times. However they quote an experimental uncertainty of approximately ±3.0 km in determining altitude from the decay time using a wavelength of 8.27 m, but find an average spread in altitude of ±4.8 km in their data and were unable to provide a conclusive account as to why this was so.

[1] It has been found [24] that the effect of the geomagnetic field is minor for most geometries

Weiss [26] also investigated the $\ln D$ vs. altitude relationship and also found unexpectedly large scatter. The main reason for the scatter postulated is a diurnal variation as well as possible small effects due to plasma resonance and the geomagnetic field.

Greenhow and Hall's [27] investigation pointed out the great dependence the scale height determined by equation (2.23) on the uncertainties assumed in the values of altitude and diffusion coefficient. They attributed the great scatter in the relationship to be due to large errors in determining the decay time of an echo.

The large scatter in the $\ln D$ vs. altitude relationship has been a feature of every investigation into this field. As yet there is still no conclusive explanation as to why the scatter should be so large. The result is that diffusion is not a satisfactory measure of the altitude of a meteor train, providing only a very approximate value.

2.2.2 Diffusion as a measure of temperature variation

Recent work by a group using the Middle and Upper Atmosphere Radar (the MU radar) at Shigaraki, Japan [28, 29, 30, 31], along with work by Jones [19], has yielded a promising new application of diffusion measurements. They have shown that a fractional temporal change in diffusion constant is approximately proportional to a fractional change in temperature. An outline of their derivation follows.

Equation(2.19) can be rewritten in the form

$$D \propto K_i T/n. \tag{2.24}$$

If we introduce small temporal variations of D, T, K, and n at a fixed height we obtain

$$\frac{D'}{D_0} = \frac{K'}{K_0} + \frac{T'}{T_0} - \frac{n'}{n_0} \tag{2.25}$$

where the subscript '0' denotes the mean values. By applying the Boussinesq approximation $n'/n_0 = -T'/T_0$ this becomes

$$\frac{D'}{D_0} = \frac{K'}{K_0} + 2\frac{T'}{T_0}, \tag{2.26}$$

finally using a proportionality constant [31] between K'/K_0 and T'/T_0 (from laboratory measurements [32]), that

$$\frac{T'}{T_0} \simeq \frac{D'}{2D_0}. \tag{2.27}$$

Using instruments with high temporal and height resolution, as well a high data rate (such as the AMOR system) this opens up the possibility of using an incoherent radar to directly measure dynamic variations in the meteor zone.

Chapter 3

System hardware, data storage and reduction

3.1 Radar hardware

The Advanced Meteor Orbit Radar has been operated by the Physics and Astronomy Department of the University of Canterbury since February 1990. The transmitter is located at the Birdlings Flat field station south of Christchurch, New Zealand (geographical coordinates 172° 39′ E, 43° 34′ S). The system is a multi-station incoherent pulse radar operating at a frequency of 26 MHz, emitting 66 μs pulses at a prf of 379 Hz and can detect meteors down to a diameter of $\sim$100 μm (corresponding to a visual magnitude of about +13). The radar is spread over 3 sites, each separated by $\sim$ 8 km: Home site (the Birdlings Flat station itself) is the location of the transmitter antenna, the home site receiving antenna and two extra antennas forming a dual interferometer. Nutt and Spit sites are the remote receiving stations and are both made up of a receiving antenna and a FM telemetry link to the home site.

Both the transmission and receiver antennas used in AMOR are co-linear arrays of total length of 40λ. This arrangement leads to narrow azimuthal fan-shaped radiation patterns. The transmitter has its main lobe pointed geographical south with the theoretical elevation maximum at 22°.9. Radiation patterns of the transmitting and receiving antennas taken together produce a theoretical beam width of $\pm 1°$ (3 dB) in azimuth and a 12° – 55° elevation range.

For elevation determination a north-south looking dual spacing interferometer is used. The two additional arrays that make up the interferometer are spaced at $3.0\,\lambda$ and $11.5\,\lambda$, providing high precision echo elevations in the range 0 – 180°, without ambiguities. The phase information is recorded using a uni-channel phase detector (to make more efficient use of storage channels than conventional HF phase detectors which require storage of both the in-phase and phase-quadrature signals). The output consists of two analog signals corresponding to the IF phase differences between signals 1-4 and 1-5. See figure (3.1) for a pictorial representation of the receiver system.

A for more detailed descriptions of both the hardware and operation of the AMOR facility see [33, 34, 35].

3.2 Data acquisition and storage

The AMOR data processing equipment deals with five video signals, the output of the three receivers plus the two phase difference signals. The analog signals are

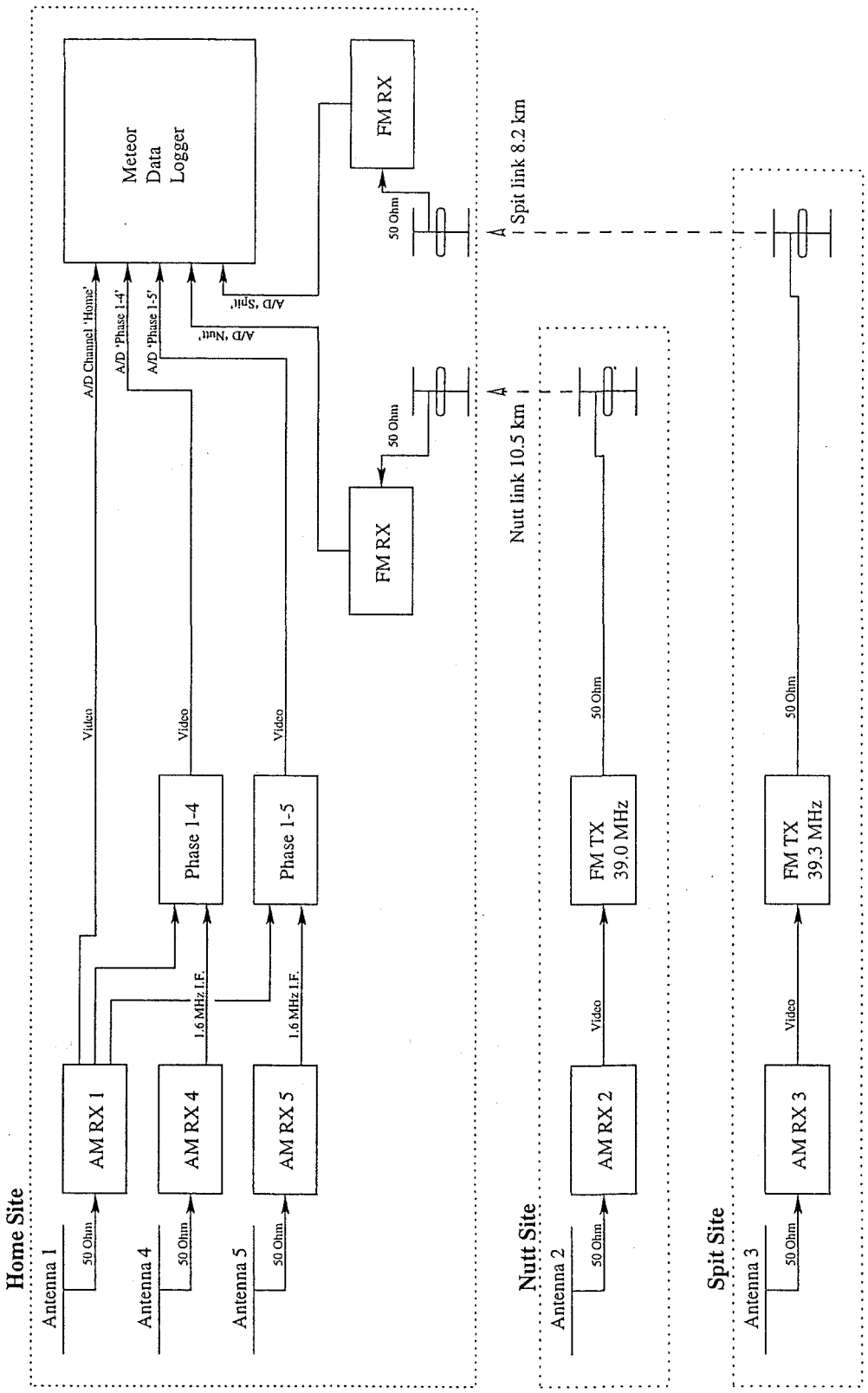

Figure 3.1: A schematic view of the AMOR receiver system showing the paths of received signals from the 5 antennas used.

digitised and placed directly into the memory of a PC (currently a 386) which is running the control program for the system. This control program has 2 main tasks; it interrupts data retrieval while the transmitter sends a pulse and detects and stores meteor echoes. A signal is judged as a detected echo if 6 consecutive sweeps produce a signal above a given threshold in the same range bin. Once this condition is fulfilled the computer stores the information from all five channels for 250 sweeps, as well as the time of occurrence. The echoes are stored in the PCs hard disk in hourly files in directories for each day, e.g. an echo detected at 01:30:24 NZST on the 3rd of February 1997 would be placed in the file NZST_01 (for all echoes between 01 and 02 hours) within the directory 970203. Periodically the data from the PC at Birdlings is transfered onto a portable hard drive and from there it can be transfered to various machines to be processed for either orbit calculation, wind measurement or some other atmospheric analysis. The NZST files are also archived, originally (1990-95) on magnetic tape and currently on DAT tape and writable CD-ROM. The yield of fully reduced meteor orbits (this being the prime function of the AMOR system) is of the order of 300 to 600 a day, depending on the time of year.

3.3 Calculation of echo decay time and diffusion coefficient

For the purposes of this project it was necessary to determine the ambipolar diffusion coefficients of meteor trains detected by the AMOR system. As the NZST files contain raw echo amplitude profiles, it was these that were used to determine the decay time constant of the echo. Equation (2.17) could then be used to give the diffusion coefficient.

The NZST files were initially processed using a modified version of the program used to filter and calculate meteoroid orbits. As this program was writen to read data off CD-ROM only the data available on CD-ROM was used, supplying data from mid 1995. The program already contained routines for doing a least mean squares fit to the exponential decay of an echo, giving the decay time constant. To be accepted for further analysis an echo had to pass a myriad of conditions ensuring that the echo was in fact due to a meteor, and had been recorded properly. For example the altitude and velocity values calculated for the meteor had lie within reasonable ranges.

Once an echo was accepted the decay time (to $1/e$ maximum amplitude) was calculated. The logarithm of the decay data is first taken and then a straight line is fitted to this using a linear least squares fit method described in 'Numerical Recipes in Pascal' [36], page 556. The routine weights the measured values of the dependent variable (the measured amplitudes in this case) based on the uncertainty of each value (see Appendix (A) for further details of this routine). The uncertainty of the amplitudes is estimated using a measure of the noise present and the amplitude of the signal at that point.

Using the data displayed in figure(3.2) and considering the general equation for

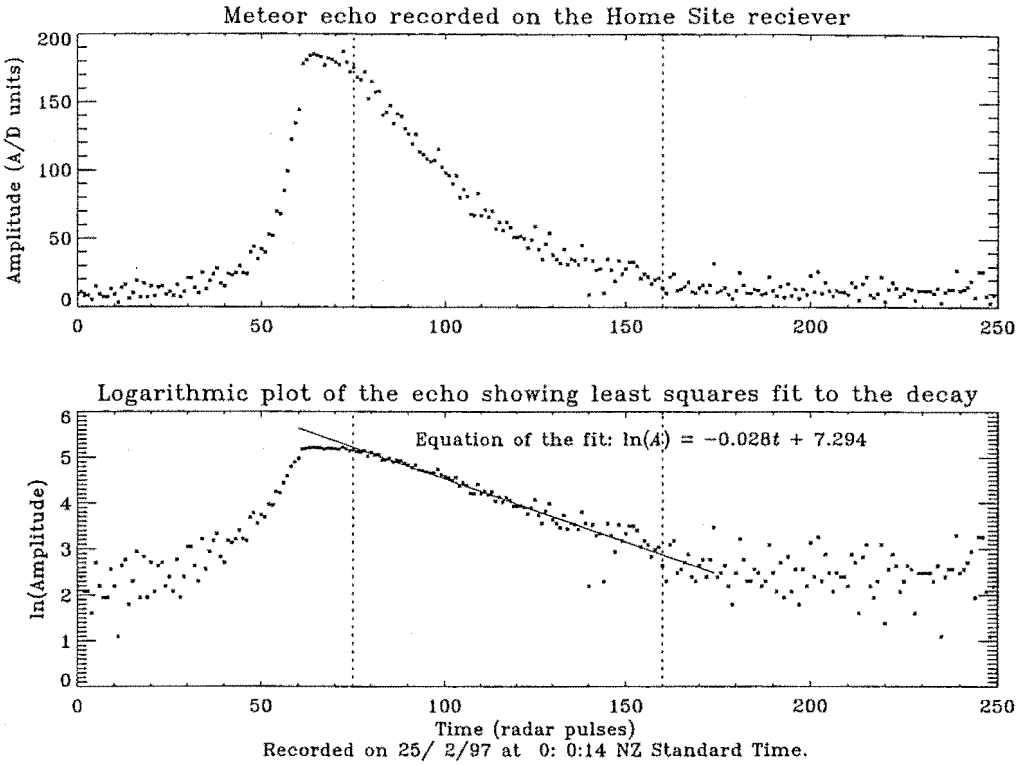

Figure 3.2: An amplitude plot of a meteor echo received by AMOR on both linear and logarithmic scales showing the method by which the decay time constant was calculated. The dotted lines indicate the starting and ending points for the fit. The spacing between radar pulses is 0.0026s.

an exponential decay,

$$A(t) = A_0 \exp\left(-\frac{t}{\tau}\right) \tag{3.1}$$

where, A_0 is the amplitude at some initial time, and τ is the decay time constant, we can see that

$$\ln(A)(t) = -t/\tau + \ln(A_0). \tag{3.2}$$

As an illustration the decay time-constant for the echo in figure(3.2) is given by

$$\begin{aligned} \tau &= -1/slope \\ &= 35 \text{ pulses} \\ &= 0.093 \text{ s.} \end{aligned} \tag{3.3}$$

As shown in section (2.1) the ambipolar diffusion coefficient D is simply related to τ. Rearranging equation (2.17) we get

$$D = \lambda^2/16\pi^2\tau \tag{3.4}$$

where λ is the wavelength of the radar being used.

In a case such as the one illustrated a value for the diffusion coefficient is easy to calculate and we can be fairly sure that it actually is ambipolar diffusion that we are measuring. However a large proportion of echoes deviate from the normal form we would expect from an underdense meteor train. To maintain a useful data rate almost all echoes showing an exponential decay must be used, whether the echoes are transitional, overdense or show strong Fresnel oscillations (see figures (3.3) and (3.4)). In all three of these cases the main complication introduced is in determining where the start and end points of the least squares fit should lie. To determine these points the profile is first numerically differentiated [33] from the maximum amplitude point on the profile to the end of the record. The maximum decay slope is then found and the point five sweeps before this is taken as the start point of the fit. The end point is taken as the point where the echo drops to an amplitude of noise plus 5 A/D units. If less than 15 data points lie between these boundaries, or the amplitude does not drop by a factor of at least $1/e$ the fit is abandoned.

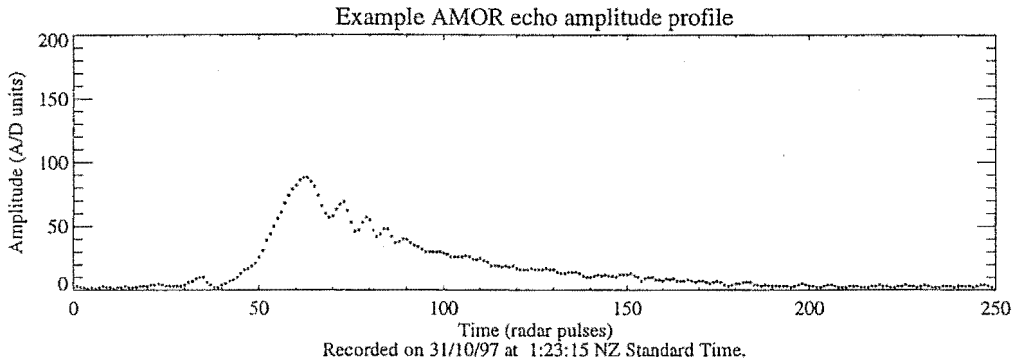

Figure 3.3: A example of an echo with Fresnel oscillations superimposed on the decay. A least squares fit through such oscillations will still provide the correct decay time constant, it is distinguishing echoes like this one from those distorted by turbulence or wind shear that proves difficult.

The maximum slope of an exponential decay occurs at it's beginning, hence starting the fit five pulses before the maximum decay slope ensures that the fit starts near the start of the exponential decay. As can be seen in figure (3.4), a transitional or overdense echo the amplitude will persist at a high level, with only a slight decrease in amplitude with time, until the train becomes sufficiently diffuse for the underdense scheme to apply. When this happens the amplitude will fall off in a rapid exponential decay - in this case the starting point of the fit will still occur at the beginning of the exponential decay as this will still be the point of maximum decay on the the profile.

To distinguish between echoes with a true exponential decay and those affected by turbulence or wind shear is the next stage. If a meteor train is distorted, large amplitude variations can result in the received echo due to the creation of multiple specular reflection points along the train. To remove such echoes while keeping those with amplitude variations due to Fresnel oscillations the differentiated profile

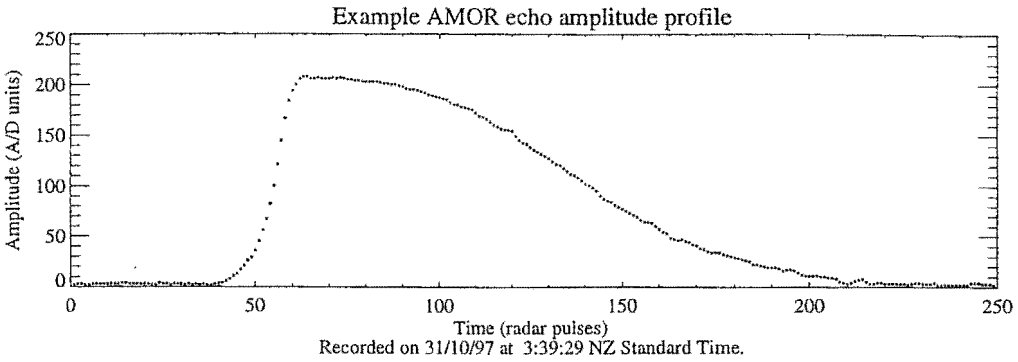

Figure 3.4: A transitional meteor echo. Notice that if the steepest point on the decay is used to determine the start of the least squares fit only the section of the echo conforming to the underdense regime will be used.

is again used. If a positive slope of more than 25% of the value of maximum decay slope is found the fit is abandoned. This test also has the effect of removing those echoes whose maximum amplitude is to low to provide reliable data as noise will often violate the criteria.

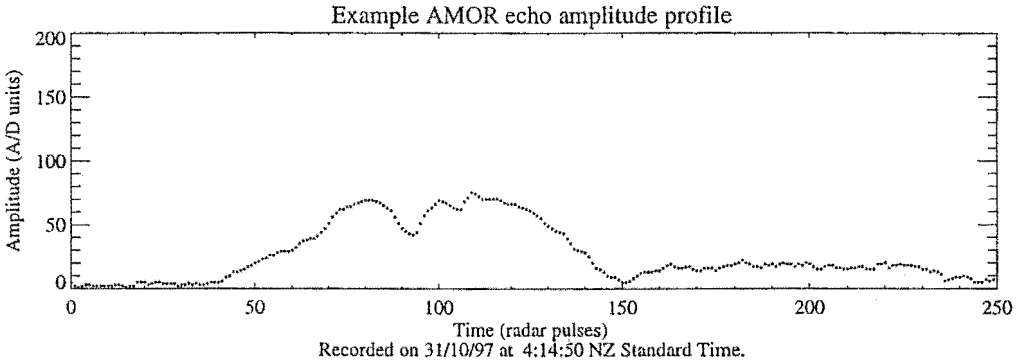

Figure 3.5: A meteor echo showing strong distortion due to turbulence and/or wind shear.

The final situation that needs to accounted for is that of a consistent rising amplitude after the maximum echo amplitude (as in figure (3.6)). Such profiles are often caused by beating between echoes from different parts of the same meteor train (again due to the train being distorted). If an echo has a region of positive derivative, the area under which is greater than 20 A/D units it is said to have a consistent rising slopes after echo maximum and the least squares fit is abandoned.

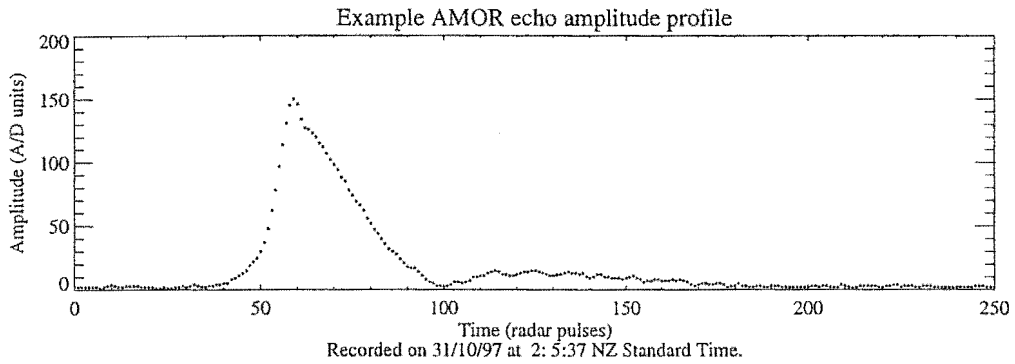

Figure 3.6: The final criteria for rejecting an echo - a region of consistently rising amplitude after the maximum echo amplitude.

Chapter 4

Diffusion coefficient vs. altitude relationship

As shown in section (2.2.1) if we assume the atmosphere is isothermal in the meteor zone (i.e. we assume a constant scale height) the ambipolar diffusion coefficient is related to the geometric altitude by the expression (equation (2.23))

$$\frac{dh}{d\ln D} = H$$

where H is the scale height. Solving this for the altitude h we get

$$h = H \ln D + C \tag{4.1}$$

where C is the integration constant. Jones and Jones [37] present values for H and C, both from theoretical calculations and empirical calculation from observations. The two formulas provided are;

$$h = 7.24 \ln D + 79.3 \tag{4.2}$$

which is derived from using theoretical ionic mobilities for Mg^+ and Fe^-, and

$$h = 5.05 \ln D + 84.1 \tag{4.3}$$

which is a fit to observational data of meteor diffusion collected by Verniani [38]. In practice all studies of meteor diffusion data have revealed a very large degree of scatter when applying equation (2.23), regardless of the measurement uncertainties of the apparatus used. Such real scatter complicates the calculation of a line of best fit. Standard linear regression fitting works by minimising the sum of the residuals between the fitted line and data points *in the dependent axis direction.* As can be seen in the plot of the AMOR data, if both the independent and dependent data both have errors associated with them, a fit of this nature is no longer adequate. Regression of one coordinate, y, on the other, x, produces a quite different slope than that obtained if we regress x on y, neither of which are the true "best fit".

The best fit can be determined by minimising the perpendicular distances from the line to the data. If we assume the coordinate uncertainties δx and δy are the same for all data, then a simple method for determining the slope of this line [39] is given by a solution of the quadratic equation

$$m^2\beta^2 - m(\beta^2 m_2 - 1/m_1) - 1 = 0 \tag{4.4}$$

where $\beta = (\delta x/\delta y)$, m_1 is the slope given by regression of y on x and, m_2 is the slope given by regression of x on y. Since all regression lines will pass through

the point $(\bar{x}, \bar{y})$ we can fully determine the true best fit line if we have the two regression lines.

To apply this analysis to the AMOR data it was necessary to have a reasonable estimation of the uncertainty in both geometric altitude and the logarithm of the diffusion constant. The uncertainty for $\ln D$ values was taken as the standard error given by all $\ln D$ data, for which the measured altitude lay between 94 and 96 km. Similarly for the uncertainty in altitude the error was taken as the standard error given by all data with $\ln D$ values between 2.0 and 2.2. This approach was taken so as to reduce the effect of any artifacts in outlying data points [1] and to ensure error values were estimated in a compatible way between the data sets. The error values found were $\delta \ln D = 0.0022$ and $\delta h = 0.0209$ respectively. The true errors in each individual measurement would almost certainly be larger than these values, however as it is only the ratio of the errors which is used by the method described above (equation(4.4)) this does not preclude their use. The β value given by these values is 0.11 which compares well with the value obtained by Howick [24] for AMOR data of 0.1.

Also, rather than a least squared deviation fit a method minimising the absolute deviation was used. With a greatly scattered data set like that found here a least absolute deviation should provide a better fit — if the squared deviation is minimised a data point with a deviation of δy from the position of the fitted line will have four times the influence on the result of the fit than a point with a deviation of $\frac{1}{2}\delta y$. Therefore outlying data will have a disproportionate effect on the slope of the line - using a least absolute deviation method removes this problem.

Figure (4.1) shows the result of doing this analysis on the entire available AMOR data set, along with the raw data and the equations given by Jones and Jones.

As can be seen the data are distributed basically as was expected. Despite the large amount of scatter the points are distributed along a linear band centered at approximately 95 km. An interesting feature of the data is the vertical band of points at $\ln D \approx 3.5$. It is almost certain that this is an artifact created when the decay time of the echo is determined (see section (3.3)). A investigation was made into finding a common feature of the echo profiles of the data in this area in the hope of filtering them out in the initial processing, however no obvious cause was found. If the use of AMOR data for providing diffusion coefficients is to become routine a more streamlined package for reducing the data will be required and this problem can be addressed.

The line of the best fit to the AMOR data has the equation

$$h = 4.83 \ln D + 84.8 \tag{4.5}$$

The disadvantage of the best fit method employed here is that it does not provide an estimate of the uncertainty in the calculated slope. It is therefore not possible to make quantitative comparisons with previous results (especially since Jones and Jones do not provide uncertainties for their calculated scale heights), but we can

[1] The ranges chosen in both altitude and $\ln D$ are centered on the mean point of the data, see figure (4.1)

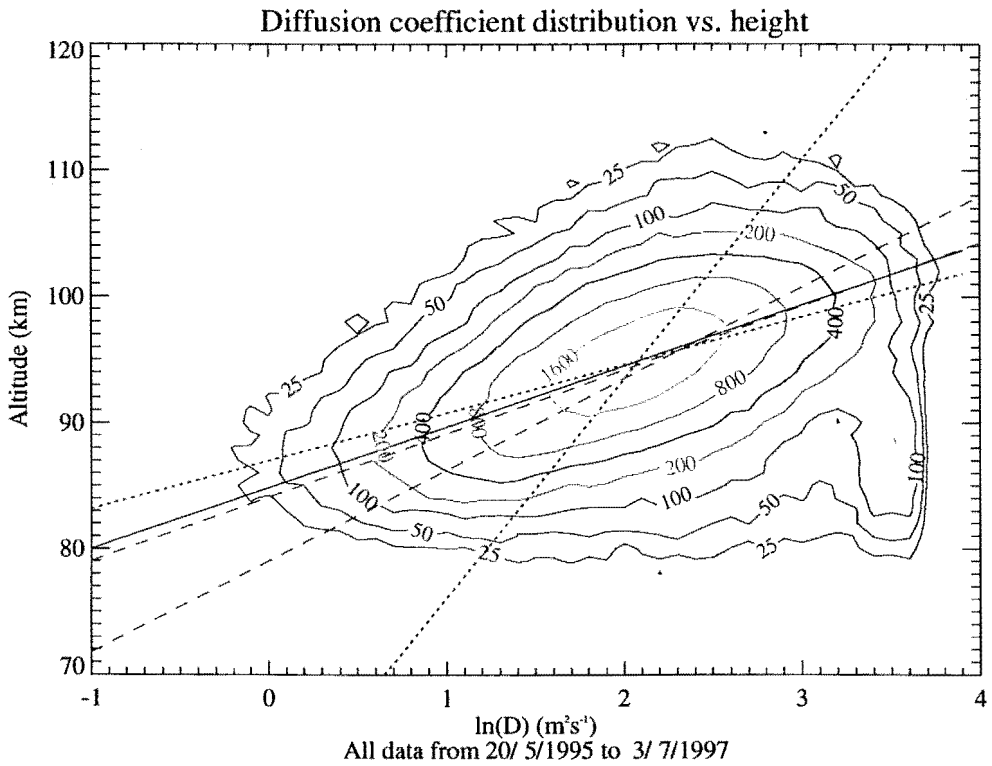

Figure 4.1: The distribution of diffusion coefficient with respect to altitude. The contours show the density of AMOR data, the values refer to how many data points are contained in each 0.1 (in $\ln D$) by 1 km bin. The dotted lines are the least absolute fits to the AMOR data, while the red solid line is the best fit. The two dashed lines are those given by equations (4.2) [green] and (4.3) [blue].

make qualitative comparisons. Compared to the scale heights given by equations (4.2) and (4.3) (of 7.24 km and 5.05 km respectively) this is comparable, particularly with that derived from Verniani's observations. Jones and Jones state that the theoretical prediction of equation (4.2) is only valid for meteors detected in the altitude range $\sim 90 - 100$ km, which limits it's usefulness as a comparison to the full AMOR data set. Applying cutoffs to the data to make a comparison between 90 and 100 km to equation (4.2) is also not practical as doing this changes the distribution of the data near the cutoff points, and thereby produces a different line of best fit [24]. It also seems likely that the artifact in the data at $\ln D \approx 3.5$ would have had some effect on the slope of the best fit line, although there are relatively few points in this region and methods used to calculate the best fit should have minimised their effect. Any effect this artifact had would have resulted in a decrease of the slope of the best fit line, hence removing the wayward data would probably result in better agreement between the AMOR data and the relationships given by Jones and Jones.

From this we can say that data set presented here shows reasonable agreement with previous results. Also it is obvious that due to the large degree of scatter in the $\ln D$ vs. h relationship the use of meteor decay times in determining the altitude of the events is only valid as an average measure over a large sample.

Chapter 5

Time series analysis

5.1 Short time scales

As discussed in section 2.2.2 recent work has shown that it is possible to use ambipolar diffusion coefficients as a measure of temperature. Using meteor diffusion measurements made by the MU radar Tsutsumi *et. al.* [29, 30] published time series of relative change in diffusion coefficient at given altitude, filtered to show only periods of 5-10 hours. That work revealed complex wave-like structure with evidence of downward phase propagation.

As already stated AMOR has good time-height resolution and so should be able to detect structure of this type. In order to determine if the AMOR system could be of use in detecting short period waves such as these a program was developed in the IDL language (see appendix (A.3)) specifically to examine the high frequency component of time series data. The program uses the 2 km altitude bins created when the data are read into IDL and processes the data for each altitude independently. The data are placed into hourly bins and a spline is fitted to interpolate any hours of missing data. The resulting vector is then passed through a low pass digital filter with a cut-off frequency corresponding to 11 hours, producing a mean diffusion curve for normalisation (a D_0 value, see section (2.2.2) and figures in this chapter). The ratio of the spline and smoothed curves is taken and stored as the normalised diffusion coefficient time series for that altitude.

Figure (5.1) gives an example of the output of this analysis for the April 10-13, 1997. The altitude range used is 89 to 101 km as outside this range the data were found to be too sparse to be useful. Figure (5.1a) shows the time series for each altitude separately with dashed lines indicating downward propagating wave-like structures. Figure(5.1b) shows the same thing, but as a contour plot. Structures like this were found throughout the data.

Both plots clearly show vertical structure in the data, particularly the contour plot with it's clearly defined narrow near vertical bands. This vertical structure is shown to be wave-like with downward phase propagation by figure (5.1a), as indicated by the dashed lines. The vertical phase speeds inferred by the slope of these lines range between about 0.05 ms^{-1} and 1.7 ms^{-1} with periods between 5 and 6 hours between successive peaks in the horizontal profile.

The many other studies into gravity wave propagation in the middle atmosphere indicate that we should expect downward phase propagation and vertical wavelengths between $\sim$ 5 and 50 km [40, 41]. A period of 5.5 hours and a propagation speed of 11 ms^{-1} corresponds to a vertical wavelength of 19.8 km, so at first inspection at least, the structures shown in figure (5.1) do agree with what we

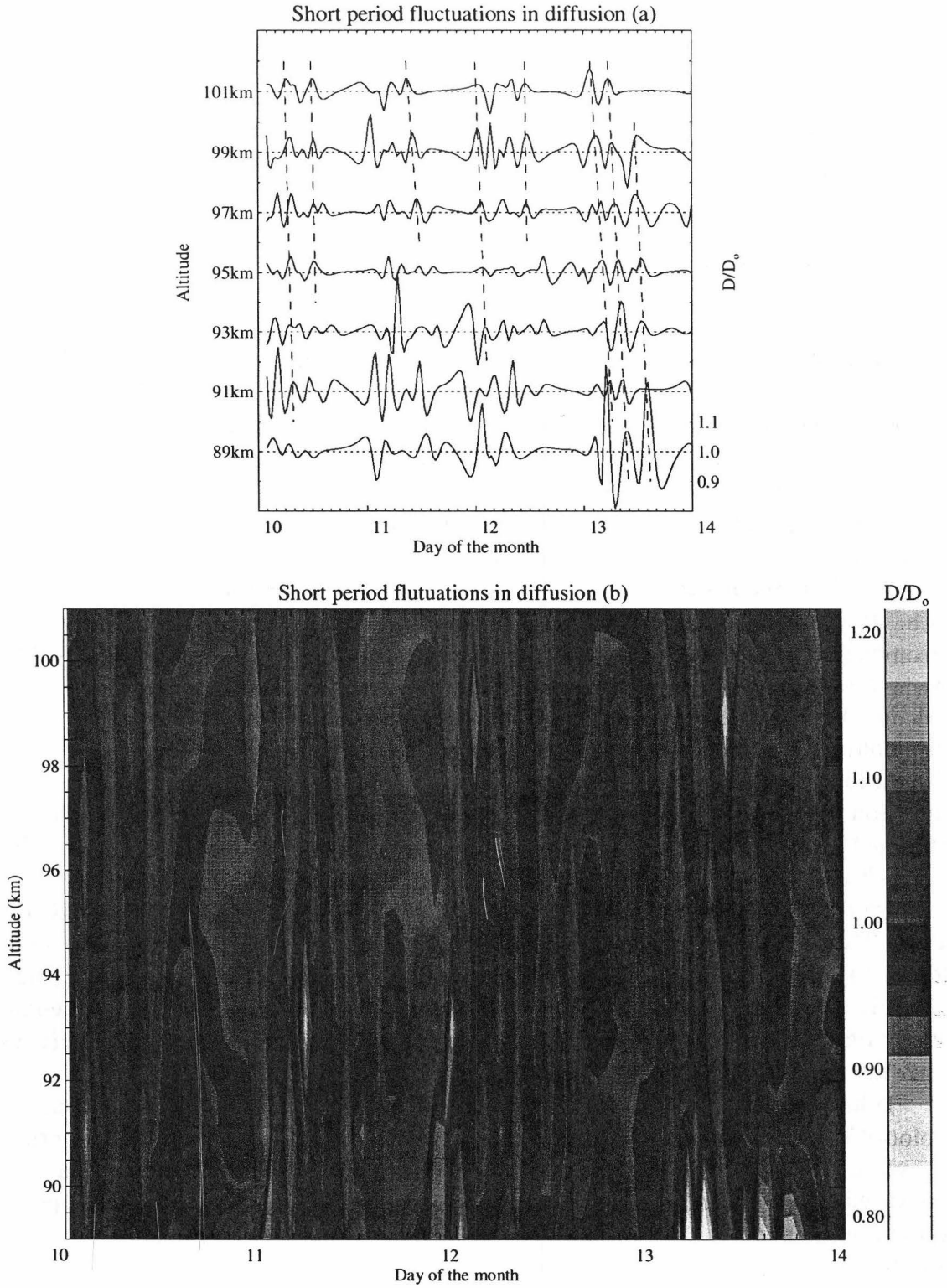

Figure 5.1: Both plots show high pass filtered time series of normalised diffusion coefficients with periods less than 11 hours as seen between April 10-14, 1997. The data is spaced a 2 km intervals vertically, and in figure (b) linear interpolation is used between each level.

would expect from gravity waves.

The parameters for those wave-like structures identified above also agree with those found by Tsutsumi *et. al.* in their investigations. Their measurements showed downward phase propagation ranging from ~ 0.6 ms^{-1} to 1.7 ms^{-1} and periods ranging from ~ 4.5 hours to 6 hours. The fact that the MU radar meteor measurements compared well with other wind measurements between 80 and 120 km shows that gravity waves in the meteor zone can be detected by radio measurements. In turn the similarity of the AMOR results to the MU radar results strongly suggest that it is indeed gravity waves that have been detected here.

As described in chapter (2) fluctuations in ambipolar diffusion are directly proportional to fluctuations in temperature (to some degree of approximation). Using equation (2.27),

$$\frac{T'}{T_0} \simeq \frac{D'}{2D_0},$$

we can see that the structures identified in figure (5.1) correspond to the range,

$$\frac{0.05}{2} \lesssim \frac{T'}{T_0} \lesssim \frac{0.1}{2}$$

or,

$$0.025 \lesssim \frac{T'}{T_0} \lesssim 0.05. \tag{5.1}$$

Taking 200 K as the temperature in the mesopause we find this corresponds to temperature changes of,

$$5 \lesssim T' \lesssim 10 \text{ K}. \tag{5.2}$$

5.2 Mid time scales

An obvious time-scale to search for oscillation in the atmosphere is on the daily basis. The Solar heating 'switch' produces strong tidal like features with periods of 24 hours and its harmonics. To isolate such oscillations averaging was used to remove random noise and higher frequency components. All data were placed into twenty four one hour bins, producing an 'average day' for each 2 km altitude bin. A multiple regression fit, weighted by the standard error in the averaged data, was then done using periods of 12 and 24 hours. The result of this can be seen in figure (5.2). The fit to the data is very good at all heights, with χ^2 values[1] between 0.03 and 0.10 and only one point not agreeing with the fitted curve within its uncertainty range.

Figure (5.2) shows an average diurnal variation, however it is known that the diurnal tide in the Mesopause region varies strongly with season [42]. The analysis was therefore repeated on a seasonal basis to reveal this, or any other, seasonal variation was being hidden by the total mean analysis. The results of this are shown in figures (5.5) to (5.8). As can be seen there is no real sign of any dependence

[1]See appendix (B)

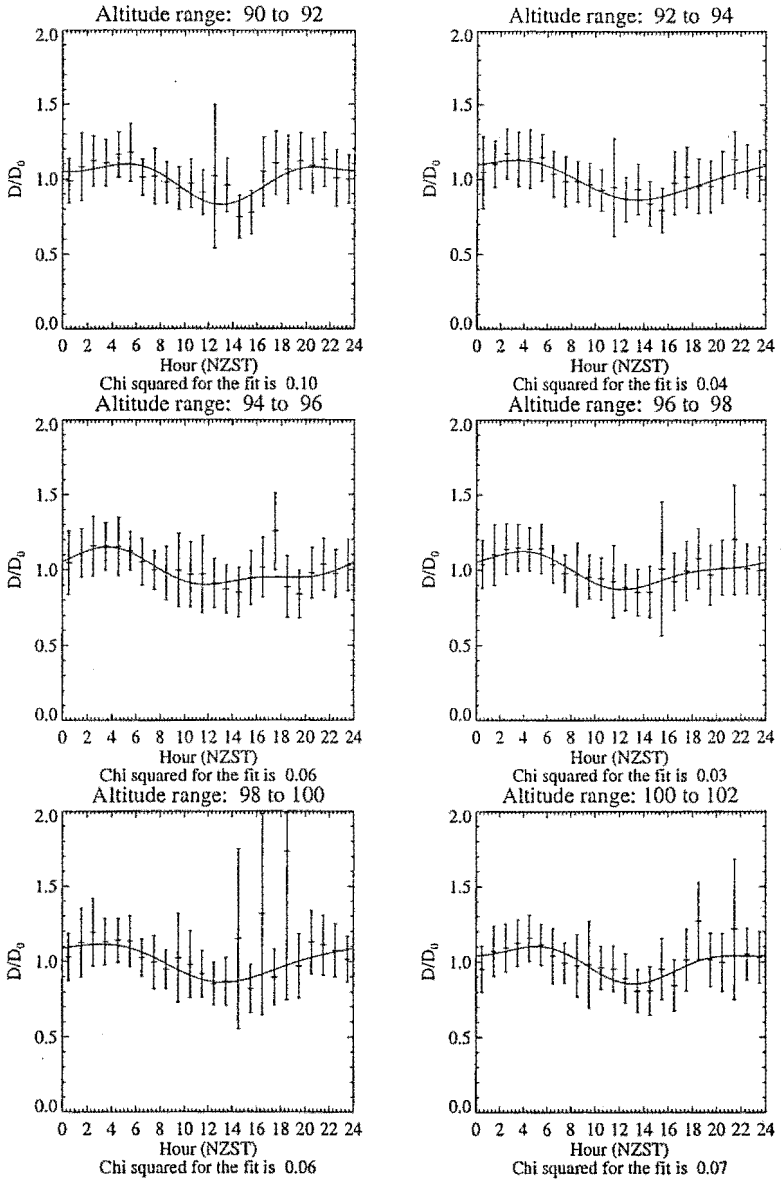

Figure 5.2: Hourly means of all data between 90 and 102 km showing mean diurnal tide. Points are plotted with error bars showing standard error $(\sigma/\sqrt{(}n))$. The curve is a weighted non-linear least squares fit using sine and a cosine curves of 12 and 24 hour periods.

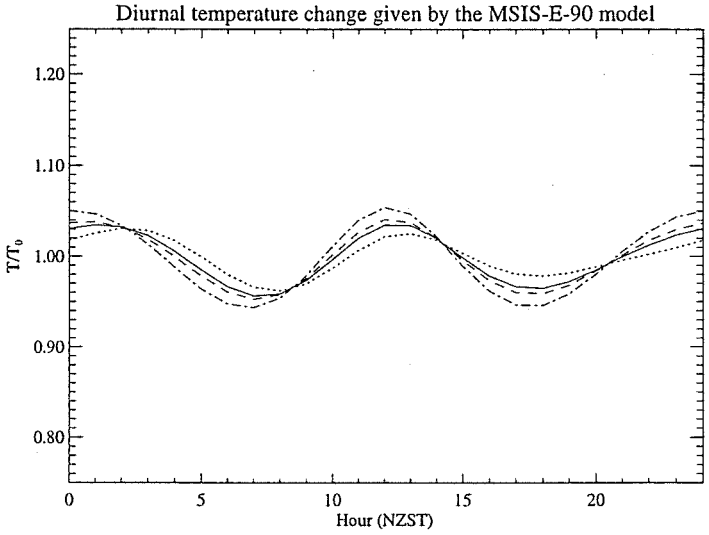

Figure 5.3: The daily relative temperature change as given by the MSIS-E-90 model. The altitude was set at 95km, and the location to that of Birdlings Flats. The four curves represent different seasons. The dashed line is for the 15/01/1996 (Summer), the solid line for the 15/04/1996 (Autumn), the dotted line for 15/07/1996 (Winter), the dash - dot line for 15/10/1996 (Spring).

on season, the increased amplitude and any phase change being most likely due to increased scatter.

To compare the measured results with what might be expected the MSIS-E-90 model developed by the Planetary Atmospheres Branch at the NASA Goddard Space Flight Center [43] was used to produce temperature profiles for characteristic days. This model is based on the MSIS-86 model of the thermosphere [44, 45] and is a analytic empirical model which aims to build a picture of conditions in the entire atmosphere based on measurements made by satellites and ground-based instruments.

The prime sources of data for the model include satellite drag, satellite mass spectrometer and ground based incoherent scatter measurements for the thermosphere/mesosphere and the MAP Handbook 16 [46] for the lower atmosphere extension. The model is available for use online at the National Space Science Data Centre's web site [2]. Figure (5.3) shows the results given by the model when run for times which should be characteristic of the AMOR data used. As can be seen the model predicts a that the semi-diurnal tide should dominate any diurnal variation (which is in agreement with observational data [42]), and that the amplitude of the tide should be roughly a 1 to 5 % change in temperature. This corresponds to ~ 2 – 10 % change in diffusion coefficient. The AMOR data shows error bars of at best ~ 0.1 in D/D_0 (or $\sim 10\,\%$ change in D) and diurnal variation of at least 1.5 in D/D_0. It seems likely then that whatever is causing the diurnal variation observed in diffusion it is not an atmospheric tide.

It is known that if altitude information is neglected and all meteor echoes considered a diurnal variation will be observed in the overall diffusion coefficients measured by a meteor radar. Meteoroids hit the morning side of the planet with greater frequency and atmospheric velocity than the afternoon/evening side of the planet. This is because the morning side of the planet faces towards the direction of the Earth's orbital motion, hence it effectively sweeps up meteoroids as the Earth moves through space. Not only will this result in more meteors being detected in the morning but they will also occur at greater heights. The faster a body is travelling when it hits the atmosphere the more quickly it will heat up and the higher an ionisation train will occur, since the diffusion rate is dependent on the atmospheric density meteor trains created higher in the atmosphere will give higher diffusion coefficients. For a more detailed explanation of this effect see [22].

Figure (5.4) demonstrates this. All the diffusion coefficients have been averaged into hourly bins, irrespective of which height they occurred at. This has then been analysed in exactly the same way as the data for the height dependent plots in figures (5.2) and (5.5) to (5.8). As can be seen there is a diurnal variation with a clear peak in the mid morning. One would expect a minimum to occur around 15:00 by the above argument but because of the greatly increased uncertainty in this region of the day it is not surprising that this is not the case. The similarity between figure (5.4) and the height dependent figures is interesting considering that the variation in measured diffusion described above should not be present in the

[2]The address is http://nssdc.gsfc.nasa.gov/space/model/models/msis.html

values *at a specific height*. No likely cause of the variation seen in figures (5.2) and (5.5) to (5.8) has been discovered, and it remains unclear whether it is due to some real atmospheric phenomena or a subtle feature of the measurement procedure.

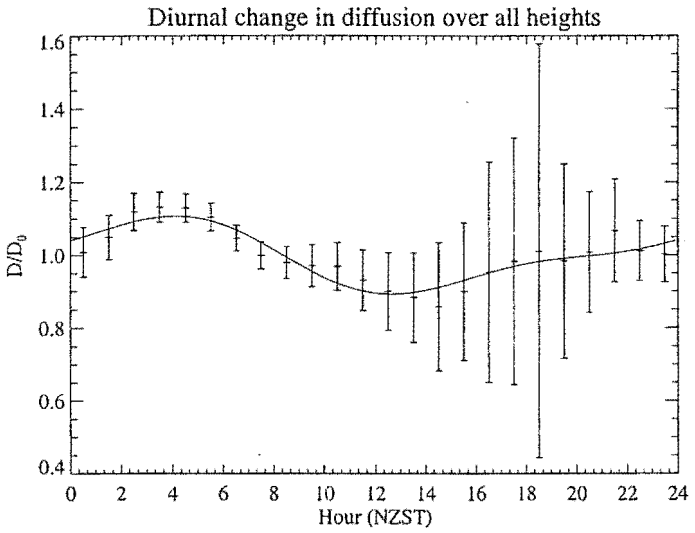

Figure 5.4: Hourly means of all meteor diffusion coefficients, irrespective of measured altitude

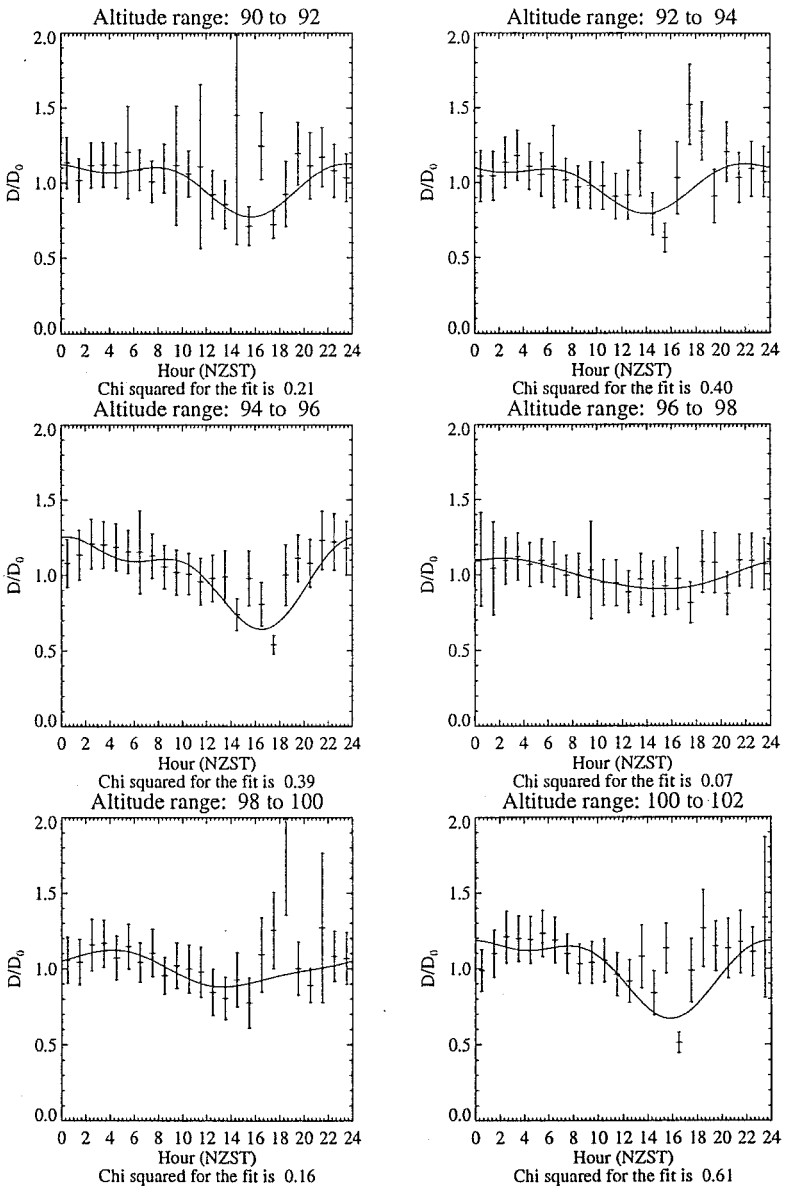

Figure 5.5: Hourly means of all data between 90 and 102 km showing mean diurnal variation for autumn. Plots were done in the same method as figure(5.2).

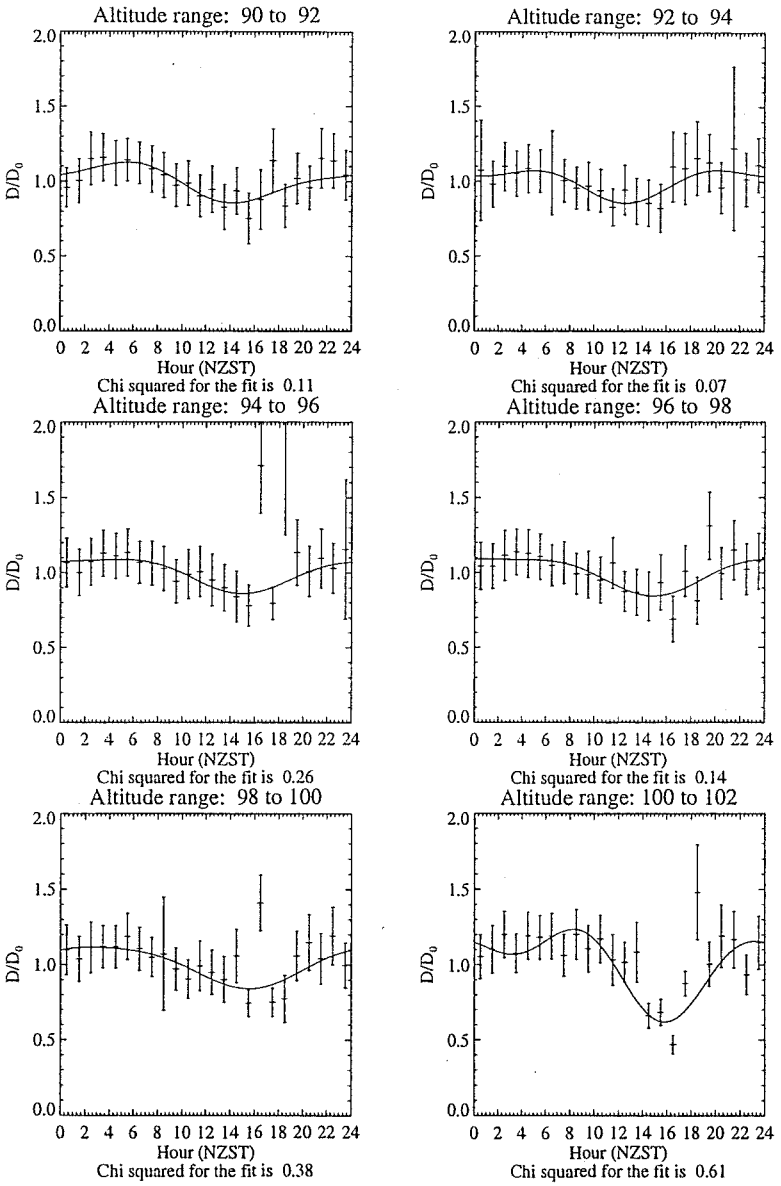

Figure 5.6: Hourly means of all data between 90 and 102 km showing mean diurnal variation for winter. Plots were done in the same method as figure(5.2).

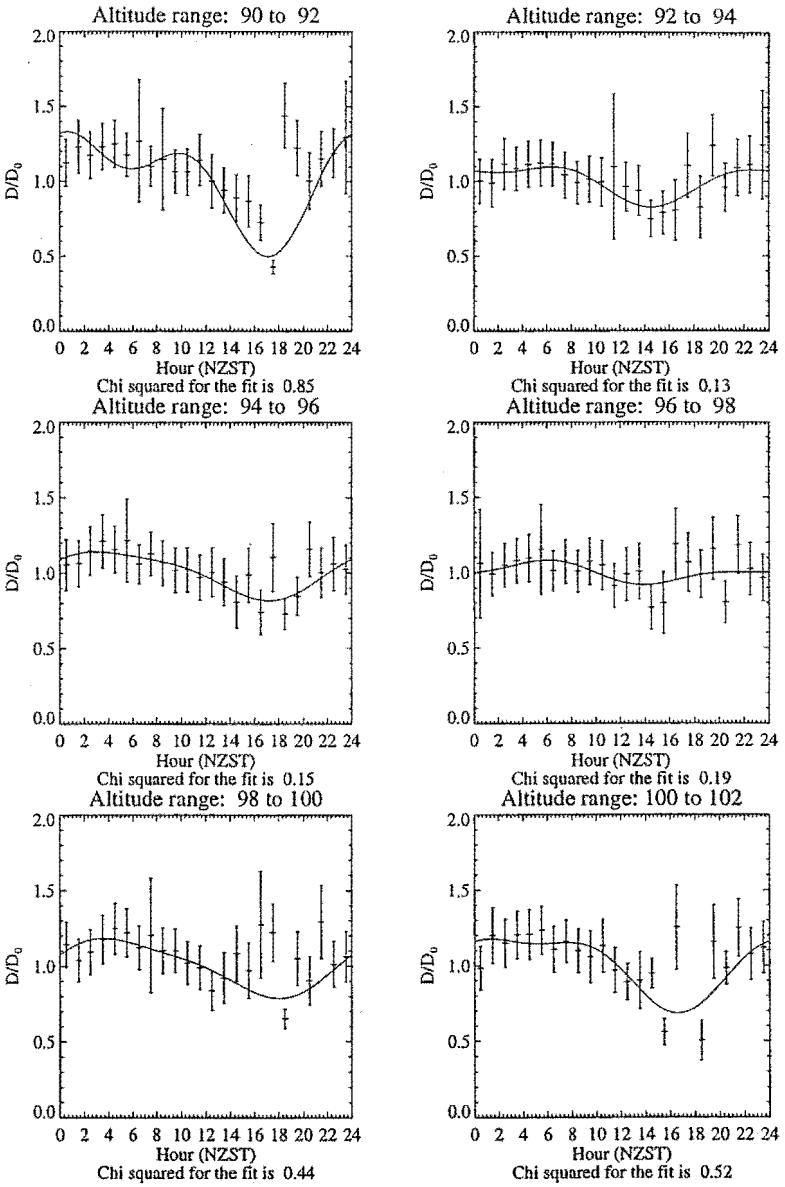

Figure 5.7: Hourly means of all data between 90 and 102 km showing mean diurnal variation for spring. Plots were done in the same method as figure(5.2).

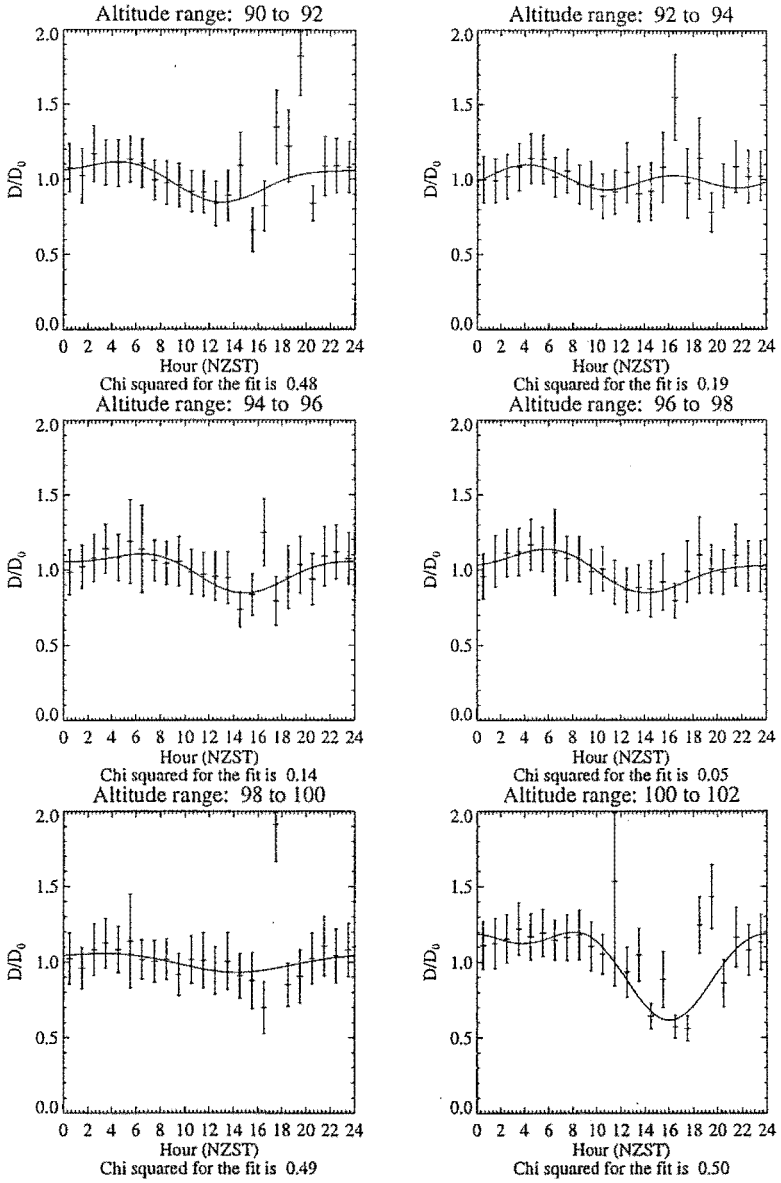

Figure 5.8: Hourly means of all data between 90 and 102 km showing mean diurnal variation for summer. Plots were done in the same method as figure(5.2).

5.3 Long time scales

The final time series analysis done on the data set was designed to detect any annual variation in the data. The data were binned on a daily basis within each 2 km altitude bin and then an unweighted regression fit of a 365.25 day oscillation was performed. The result of this is shown in figures (5.9) and (5.10) for the ten altitude bins between 84 and 104 km.

As can be seen the annual oscillation is almost completely masked by scatter, but a annual cycle has still been found by the regression routine. Above 92 km the cycle has a maximum at near midyear (i.e. in winter) whereas below this the cycle suddenly switches, giving a maximum in the summer months.

It is well known that both the temperature profile and zonal wind undergo a reversal near the mesopause (see section (1.4.1) and figure (1.2)). At lower altitudes there is a temperature maximum in the summer months and a minimum in winter, higher up this is reversed. As can be seen this is in agreement with figures (5.9) and (5.10) with a clear maximum in D/D_0 near the new year at 91 km altitude and below, and a minimum in the same time region for altitudes 95 km and up. Figure (1.2) shows the reversal in temperature gradient occurring at the relatively low height of $\sim$ 70 km, which is not what is suggested by the AMOR data, however the altitude of this switch is by no means fixed. It seems reasonable to postulate that the reversal in the phase of the annual variation shown in figures (5.9) and (5.10) is the result of the change in zonal temperature profile shown in figure (1.2).

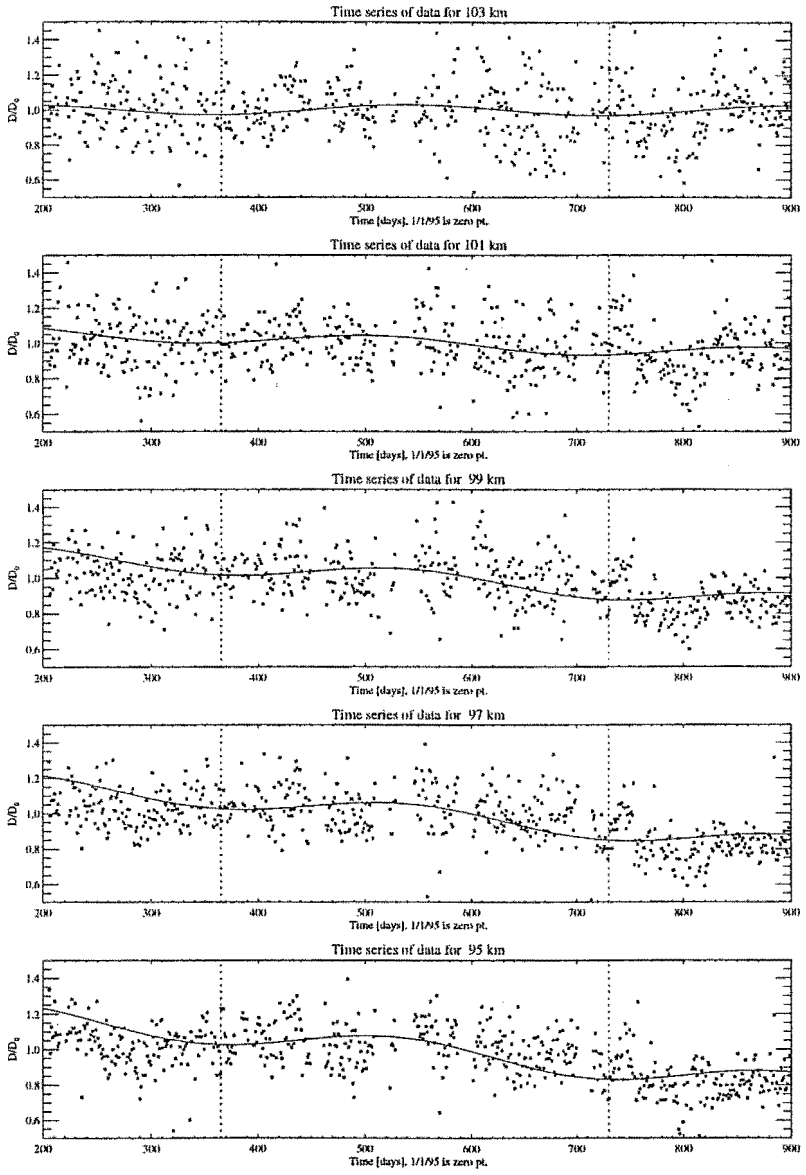

Figure 5.9: Daily binned data for all data from late July 1995 to July 1997. The vertical scale is again relative change in diffusion coefficient, this time with the mean value taken over the entire data set.

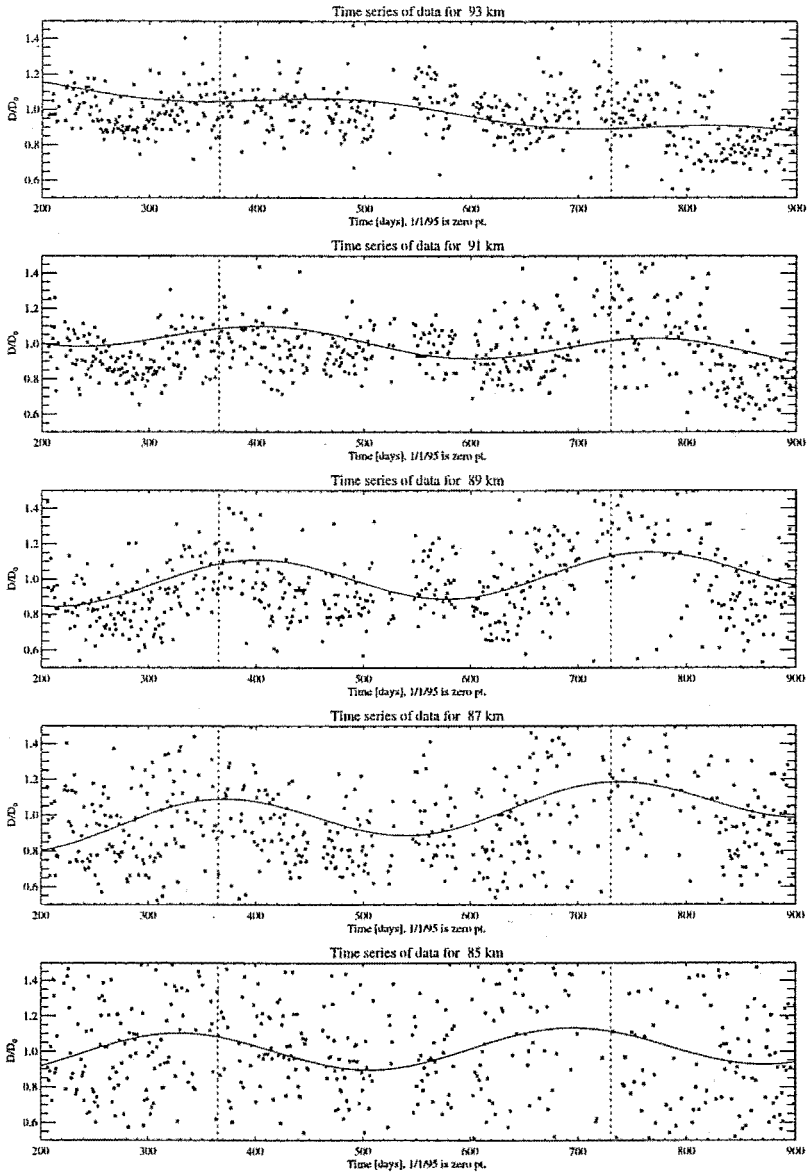

Figure 5.10: Daily binned data for all data from late July 1995 to July 1997.

Chapter 6

Conclusions

This work reports an investigation into the suitability of the AMOR incoherent multi-station meteor radar system to provide useful information on wavelike structures near the mesopause (80 – 100 km in altitude) using the measured ambipolar diffusion coefficient of meteor trains. Pre-existing code was modified to produce a large body of meteor echo decay time constants covering a time period of approximately 2 years starting in mid 1995.

Software was developed in the IDL language to calclate ambipolar diffusion cofficients from the decay times, investigate both the altitude vs. diffusion coefficent relationship and time series dependence of the diffusion data, and provide graphical representation of the results.

As with previous studies a very large degree of real scatter was found in the altitude vs. diffusion coefficent relationship when compared to a simple theoretical model. No investigation was made into this cause of this scatter as there have been many causes suggested in the past (see [24, 25, 27, 47]). A linear fit was done to the the data, taking into account the uncertainty in both altitude h and the logarithm of the diffusion coefficient $\ln D$. This was then used to give a scale height of $H = 4.8$ km for the atmosphere between $\sim 80 - 110$ km using the theoretical relationship $h = H \ln D + C$. This was compared to values given by Jones and Jones [37] and found to be in good agreement.

The time series analysis of the data was done over three different period regimes; short period oscillations of less than 12 hours, tidal waves of $\frac{1}{2}$ to 1 day, and annual variation. Evidence of waves with ~ 6 hour period showing downward phase propagation were detected by the short time scale analysis. It is postulated that these are gravity waves as detected by the MU radar at Shigaraki Japan [29, 30]. The possibility of using the AMOR system to monitor gravity wave propagation near the mesopause is therefore real, however providing an automated system for detecting gravity wave-like structures in the data and determining parameters such as wavelength, amplitude and vertical phase speed will provide significant challanges for future workers.

The analysis of the data on time scale periods of the order of a day produced inconclusive results. There the AMOR data showed a weak diurnal variation with a maximum near midnight. Contrary to what might be expected there was no evidence of a semi-diurnal tide, or a seasonal dependance of the diurnal tide. Comparison to the MSIS-E-90 model shows that the predicted diurnal/semi-diurnal variation in temperature is well below the uncertainty margin of the AMOR data. It therefore seems likely that measurement of tidal variation by the method employed here is not practical.

Long time scale analysis of the data set showed a noticable variation in D/D_0, particularly over the 85 – 91 km altitude range. The annual variation found showed a change in phase of $\sim 180°$ at approximately 93 km, which is in agreement with the known temperature structure near the mesopause.

From these time series analyses it would appear that using ambipolar diffusion data from the AMOR system to detect dynamical processes near the mesopause is indeed possible. The system provides sufficient data to detect wavelike structures with periods down to a few hours, and to follow the evolution of these structures over a few days.

During the latter part of this project the data reduction routines have been upgraded to improve the geometric height determination capabilities of the system, increasing the number of usable echoes by about a factor of five. With this improvement and a more streamlined reduction package for determining the decay life times of the echoes it is believed the AMOR system should provide useful data on gravity wave propogation between 90 and 100 km.

Although this study was unable to clearly detect tidal oscillations in the data this may be possible using the increased data set supplied by the improved altitude determination now avalible. The long period analysis of shows the potential for the AMOR data set (which contains data back to 1990) to provide a long term picture of the temperature structure of the mesosphere region.

Appendix A

Program listings

This appendix lists some of the code used in this work. The listings are basically as they were used, however all plotting and other output code has been removed.

The two languages used in this work were Borland Turbo Pascal and IDL from Research Systems Inc. Turbo Pascal is improved version of Pascal for standard PCs running DOS. It produces stand alone compiled programs and was used to produce the control, data collection and data reduction programs of the AMOR system.

IDL is a high level interpretive language. Programs are run one line at a time in the IDL programming environment — an application that is available for all commonly used computer systems. It provides a powerful and user friendly system for data analysis and was used for all the analysis specific to this project.

A.1 The calculation of diffusion time

The Turbo Pascal procedure for calculating the slope of the decay of ln(amplitude) (see section (3.3)) is given below. The main body of this procedure is taken directly from 'Numerical Recipes in Pascal' [36]. This procedure is basically the heart of the Turbo Pascal program used to do the initial analysis of the data.

```
PROCEDURE fit(Amp: IntVector; Istart,Iend: byte; mwt: integer;noise:byte;
         VAR a,b,siga,sigb,chi2,q: real);
VAR
   x    : array[1..250] of byte;
   y    : array[1..250] of real;
   sig  : array[1..250] of real;
   i    : integer;
   wt,t,sy,sxoss,sx,st2,ss,sigdat: real;
BEGIN
{The value of x is just the indexes..}
ndata:= abs(Iend-Istart);

{Create dummy values for ocations where decay is extremely short}
if (ndata < 3) THEN BEGIN
   a:= 0{999}; b:= 999; siga:= 999; sigb:= 999; chi2:= 999; q:= 999;
END ELSE BEGIN

FOR i:= Istart to Iend DO
   x[i]:=i;

{The y values are the logs of the amplitudes..}
             BEGIN
```

```
FOR i:= Istart to Iend DO BEGIN
   IF Amp[i] = 0 THEN
      y[i]:= 1
   ELSE
      y[i]:= ln(Amp[i]);
END;
              END;

IF (Noise < 1) THEN Noise:= 1;
              BEGIN
FOR i:= Istart to Iend DO BEGIN

{Estimate uncertanties in ln(amplitude)}
   IF (Amp[i] <= 5) THEN
      sig[i]:=noise/10
   ELSE
      sig[i]:= noise/(2.5*(Amp[i]));
END;
              END;

sx := 0.0; sy := 0.0; st2 := 0.0; b := 0.0;
IF (mwt <> 0) THEN BEGIN
   ss := 0.0;
   FOR i := Istart TO Iend DO BEGIN
      wt := 1.0/sqr(sig[i]); ss := ss+wt; sx := sx+x[i]*wt; sy :=sy+y[i]*wt
   END
END ELSE BEGIN
   FOR i := Istart TO Iend DO BEGIN
      sx := sx+x[i]; sy := sy+y[i] END; ss := ndata
   END;
   sxoss := sx/ss;
   IF (mwt <> 0)THEN BEGIN
      FOR i := Istart TO Iend DO BEGIN
         t := (x[i]-sxoss)/sig[i]; st2 := st2+t*t; b := b+t*y[i]/sig[i]
      END
   END ELSE BEGIN
      FOR i := Istart TO Iend DO BEGIN
         t := x[i]-sxoss; st2 := st2+t*t; b := b+t*y[i]
      END
   END;
   b := b/st2; a := (sy-sx*b)/ss; siga := sqrt((1.0+sx*sx/(ss*st2))/ss);
   sigb := sqrt(1.0/st2);

   chi2 := 0.0;
   IF (mwt = 0) THEN BEGIN
      FOR i := Istart TO Iend DO BEGIN
         chi2 := chi2+sqr(y[i]-a-b*x[i])
      END;
      q := 1.0; sigdat := sqrt(chi2/(ndata-2)); siga := siga*sigdat;
      sigb := sigb*sigdat
   END ELSE BEGIN
      FOR i := Istart TO Iend DO BEGIN
         chi2 := chi2+sqr((y[i]-a-b*x[i])/sig[i])
      END;
```

```
      q := gammq(0.5*(ndata-2),0.5*chi2)
   END;
END;                    { end of usual case of > 3 data values}
END;
```

A.2 Diffusion coefficient vs. altitude calculation: `dalt.pro`

The following is a listing of the program used to calculate the atmospheric scale height from the AMOR diffusion data, as well as preparing the data and various equations for plotting. The program starts by calculating $\ln D$ from the raw diffusion coefficient array `D`. The $\ln D$ values are then binned in a three dimensional array (using the `histogram` routine) for plotting. Next the lines given by Jones and Jones are then computed so that they can be plotted latter. The least absolute deviation fits are then done on the AMOR data set using the IDL routine `ladfit` and these are then used to calculate the slope of the best fit `m2`.

```
tmp = where(D gt 0)
ii = tmp MOD n_data
jj = fix(tmp/n_data)
lnD = alog(D(ii,jj))
h = alt(ii,jj)

barray = intarr(50,50)
h2 = indgen(50) + 70.0
D2 = findgen(50)/10 - 1

for j = 0,49 do begin
   tmp = where(h ge h2(j) and h lt h2(j)+1)
   kk = tmp MOD n_elements(ii)
   ll = fix(tmp/(n_elements(ii)))
   lnD2 = lnD(kk,ll)
   barray(*,j) = histogram(lnD2, max = 4, min = -1, binsize = 0.1)
endfor

; Theory based Dalt from Jones and Jones
lnDth = alog(10)*(0.06*h2 - 4.74)

; Experimentally based Dalt from Jones & Jones
lnDex = alog(10)*(0.086*h2 - 7.23)

; Do 2 ''least absolute deviation" fits to AMOR data
coef = ladfit(lnD,h)
coef2 = ladfit(h,lnD)

fit = coef(0) + coef(1)*D2
fit2 = coef2(0) + coef2(1)*h2

; Now calculate slope of best fit line
tmp = where(h gt 94 and h lt 96)
mom = moment(lnD(tmp))
dlnD = sqrt(mom(1))/(sqrt(n_elements(lnD(tmp))))
tmp = where(lnD ge 2.0 and lnD lt 2.2)
```

```
mom = moment(h(tmp))
dh = sqrt(mom(1))/(sqrt(n_elements(h(tmp))))

a = (dlnD/dh)^(2)
b = (dlnD/dh)^(2)*coef2(1) - 1.0/coef(1)

m2 = (-b - sqrt(b^2 - 4.0*a)) / (2*a)

end
```

A.3 Short time scale analysis: filter.pro

The program used for the analysis found in section (5.1) is listed below. Each 2 km altitude bin is analysed independantly and the data is placed into 1 hour bins. Once the time binning has been done and the null data has been removed a spline is fitted to the data to interpolate any missing hours of data. The spline is then passed through a low pass filter to provide with a cut off frequency corresponding to 11 hours, this is then used to provide D_0 values to calculate the D/D_0 array for plotting.

```
print, 'Enter a lower altitude bin followed by a upper altitude bin $
(71, 73, 75, ...., 119 km)'
read, level1
read, level2
bot_lev = level1
p=0

; Time binning section

if date(0,0) MOD 4 eq 0 then begin
    tbins = ((date(0,n_data-1)-date(0,0))*366 + date(3,n_data-1) - $
        date(3,0))*24
endif else begin
    tbins = ((date(0,n_data-1)-date(0,0))*365 + date(3,n_data-1) - $
        date(3,0))*24
endelse

dhrbin = fltarr(tbins)
Dbin = dhrbin
Dbinsig = dhrbin
Dbinerr = dhrbin
resultarray = fltarr(tbins,((level2-level1)/2)+1)
dhrbin = findgen(tbins) + 0.5


count = -1

while level1 le level2 do begin          ;Begining of altitude
                                         ;incrementing loop
count = count+1

m=0
```

```
while level1 gt altbin(m) do m = m+1

a = where(binindx eq m)
i = fix(a MOD n_data)
Draw = D(a)
if date(0,0) MOD 4 eq 0 then begin
    dhrraw = dhr(a) + 24*((date(0,n_data-1)-date(0,0))*366 + $
        date(3,i) - date(3,0))
endif else begin
    dhrraw = dhr(a) + 24*((date(0,n_data-1)-date(0,0))*365 + $
        date(3,i) - date(3,0))
endelse

i=0
q=0

for i = 0,tbins-1 do begin
    tmp = (dhrraw ge (dhrbin(i)-0.5))*(dhrraw lt (dhrbin(i)+0.5))
    h = total(tmp)
    if h ge 2 then begin
        Dbin1 = fltarr(h)
        a = where((dhrraw ge (dhrbin(i)-0.5)) and (dhrraw lt (dhrbin(i)+0.5)))
        Dbin1 = Draw(a)
        Dmom = moment(Dbin1)
        Dbin(i) = Dmom(0)
        Dbinsig(i) = Dmom(1)
        Dbinerr(i) = sqrt(Dmom(1))/sqrt(h)
    endif else begin
        Dbin(i) = 0
        Dbinerr(i) = 0
    endelse
endfor

x = where(Dbin ne 0 and abs(Dbinerr) lt 10)

if n_elements(x) lt tbins/3 then begin
    rawarray(*,count) = 0
    resultarray(*,count) = 0
    goto, rubbish
endif

Dbin2 = Dbin(x)
Dbin2sig = Dbinsig(x)
Dbin2err = Dbinerr(x)
dhrbin2 = dhrbin(x)

Dspl = spline(dhrbin2, Dbin2, dhrbin)

;Smoothing with a digital filter
fltcoeff = digital_filter(0, 0.18181818, 50, 4)
Dlpf = convol(Dspl, fltcoeff)
Dlpf = 1.4 * Dlpf

Ddif = Dlpf
```

```
a = where(Dlpf gt 0)
Ddif(a) = Dspl(a)/Dlpf(a)
a = where(Dlpf le 0)
Ddif(a) = Ddif(a-1)
Ddif(0) = 0

resultarray(*,count) = Ddif      ;Contains data to be plotted

rubbish:                         ;landing point for lack of data goto

level1 = level1 + 2

endwhile                         ;end of altitude incrementing loop
end
```

A.4 Mid time scale analysis: average.pro

Below is the program used to calculate the average daily variation in D/D_0 (figure (5.2). The analysis for figures (5.4) to (5.8) was similar to this. Once again each altitude is analysed separately. The data is placed into one hour bins and then a multiple linear regression fit is done using the IDL routine regress using sine and cosine functions of 12 and 24 hour periods. The plotting was done inside the altitude incrementation loop, but the plotting commands have not been included in this listing.

```
p=0

print, 'Enter a lower altitude bin followed by a upper altitude bin $
(71, 73, 75, ...., 119 km)'
read, level1
read, level2

while level1 le level2 do begin  ;begining of altitude incrementing loop

m=0
while level1 gt altbin(m) do m = m+1

p = where(binindx eq m)

Draw = D(p)
dhrraw = dhr(p)
p = where(Draw gt 0)
Draw = Draw(p)
dhrraw = dhrraw(p)


; now do time bining of values (using 1 hour bins)
tbins = 24
dhrbin = fltarr(tbins)
Dbin = dhrbin
Dbinvar = dhrbin
Dbinerr = dhrbin
```

```
dhrbin = findgen(24) + 0.5

i=0
q=0
for i = 0,tbins-1 do begin
   h = where(dhrraw ge (dhrbin(i) - 0.5) and dhrraw lt (dhrbin(i) + 0.5))
   if n_elements(h) gt 1 then begin
      Dbin1 = Draw(h)
      Dmom = moment(Dbin1)
      Dbin(i) = Dmom(0)
      Dbinvar(i) = Dmom(1)
      Dbinerr(i) = sqrt(Dmom(1))/sqrt(n_elements(h))
   endif else begin
      Dbin(i) = 0
      Dbinerr(i) = 0
   endelse
endfor


; Do a non-linear least squares fit with semidiurnal and diurnial oscilations
h = where(Dbin ne 0)
dhrbin2 = dhrbin(h)
Dbin2 = Dbin(h)
Dbin2err = Dbinerr(h)
Dbin2var = Dbinvar(h)

nterms = 4
nz = size(dhrbin2)
npts = nz(1)
xdhr = fltarr(nterms, npts)

xdhr(0,*) = sin(dhrbin2(*) *2*!pi/24)      ;daily cycle
xdhr(1,*) = cos(dhrbin2(*) *2*!pi/24)
xdhr(2,*) = sin(dhrbin2(*) *2*!pi/12)      ;12 hour cycle
xdhr(3,*) = cos(dhrbin2(*) *2*!pi/12)

  Wgt = 10/Dbin2var
  a0 = fltarr(1)
  Ft = a0 & Rm = a0 & Chi = a0
  coef = fltarr(nterms) & R = coef & sig = coef
  yf = fltarr(npts)

nlcoeffs = regress( xdhr, Dbin2, Wgt, yf, a0, sig, Ft, R, Rm, Chi )

; Produce arrays for plotting
xvals = findgen(10*tbins)/10

nllsq = a0 + $
   nlcoeffs(0) * [sin(xvals *2*!pi/24)] + $
   nlcoeffs(1) * [cos(xvals *2*!pi/24)] + $
   nlcoeffs(2) * [sin(xvals *2*!pi/12)] + $
   nlcoeffs(3) * [cos(xvals *2*!pi/12)]

;Find average value for calculation of D/Do
```

```
tmp = moment(nllsq)
dDerr = sqrt(Dbin2var + tmp(1))/n_elements(Dbin2)
dnllsq = nllsq / tmp(0)
dD = Dbin2 / tmp(0)

level1 = level1 + 2

endwhile                ;end of altitude incrementing loop

end
```

A.5 Long term analysis: tseries.pro

The final analysis program, that which does the long term analysis, is listed below. As with the previous two programs the analysis of each altitude level is independant. Once again time binning is done first, this time on a daily basis. A new time array is created in which each record has it's time of occurance stored as the number of hours since the start of the data record. This is then used to bin the data.

As with average.pro a curve is fitted using the regress routine, after missing days of data have been linearly interpolated. In this case the curves fitted are a straight line and sine and cosine curves of one year period. Again the plotting was done within the altitude incrementing loop.

```
level = 93
while level ge 85 do begin      ;start of altitude incrementation


; Time binning section

tbins = 0
yr = date(0,n_data-1)-date(0,0)
if yr ge 1 then begin
   for i = 0,yr-1 do tbins = tbins + 365 + (((date(0,0)+i) MOD 4) eq 0)
   tbins = tbins + date(3,N_data-1)
endif else begin
   tbins = date(3,N_data-1) - date(3,0)
endelse


; Put data in daily bins
dhrbin = 24*findgen(tbins) + 12
Dbin = fltarr(tbins)
Dbinvar = dhrbin
Dbinerr = dhrbin

m=0
while level gt altbin(m) do m = m+1

a = where(binindx eq m)
Draw = D(a)
```

```
; Create new array that stores the time of an echo in an hour format
dhrraw = dblarr(n_data,max)
if yr ge 1 then begin
   for k = 0,yr do begin
      b = where(date(0,*) eq (date(0,0)+k))
      tmp = dhr(b,*)
      tmp(*,0) = 24*((((date(0,0)+k) MOD 4) eq 0) + 365*k + date(3,b))
      for l=1,max-1 do tmp(*,l) = tmp(*,0)
      dhrraw(b,*) = double(dhr(b,*) + tmp)
   endfor
      dhrraw = dhrraw(i,j)
endif else dhrraw = long(dhr(i,j) + 24*(date(3,i)-date(3,0)))

i=0
q=0

; Bin data into day long bins
for i = 0,tbins-1 do begin
        tmp = (dhrraw ge (dhrbin(i) - 12)) * (dhrraw lt (dhrbin(i) + 12))
        h = total(tmp)
        if h ge 2 then begin
                a = where((dhrraw ge (dhrbin(i) - 12)) and $
                          (dhrraw lt (dhrbin(i) + 12)))
                Dbin1 = Draw(a)
                Dmom = moment(Dbin1)
                Dbin(i) = Dmom(0)
                Dbinvar(i) = Dmom(1)
                Dbinerr(i) = sqrt(Dmom(1))/sqrt(h)
        endif else begin
                Dbin(i) = 0
                Dbinerr(i) = 0
        endelse
endfor

Dbin = Dbin*(Dbinerr lt 5)
Dbinerr = Dbinerr*(Dbinerr lt 5)
Dbinvar = Dbinvar*(Dbinerr lt 5)

; Create arrays without null data
a = where(Dbin ne 0)
dhrbin2 = dhrbin(a)
daybin = dhrbin2/24             ;Store time as days
daybin2 = dhrbin/24
Dbin2 = Dbin(a)
Dbinerr2 = Dbinerr(a)
Dbinvar2 = Dbinvar(a)

mom = moment(Dbin2)
dD = Dbin2 / mom(0)
dDerr = (Dbinvar2 + mom(1))/n_elements(Dbin2)

; Do linear interpolation through the vector to enable regression
Dbinr = interpol(dD,daybin,daybin2)
```

```
x = [ transpose(daybin), $
      transpose(cos((2*!pi *daybin)/365.25)), $
      transpose(sin((2*!pi *daybin)/365.25)) ]
weights = replicate(1.0, n_elements(Dbin2))
yrwave = regress(X,dD,weights,yrwavefit,const, /relative_weight)

level = level-2
endwhile                          ;end of altitude incremation

end
```

Appendix B

The χ^2 parameter

The χ^2 (or "chi-square") statistic is used in this work as a measure of "goodness of fit". It is given by the equation

$$\chi^2 \equiv \sum_{i=1}^{N} \left(\frac{y_i - y(x_i; a_1 .... a_M)}{\sigma_i} \right)^2 \tag{B.1}$$

where we have N data points (x_i, y_i) (with standard deviations σ_i) and we are fitting a function y with M parameters, a_i.

As we are trying to minimise the difference between the data and the fitted function the smaller the value of the chi-square the more closely the data is described by the function. See any of the Numerical Recipes series (for example Numerical Recipes in Pascal [36]) for a more detailed description of all aspects of the modelling of data.

References

[1] A. D. Taylor, W. J. Baggaley, and Steel D. I. Discovery of interstellar dust entering the earth's atmosphere. *Nature*, 380:323 – 325, 1996.

[2] F. A. Lindemann and G. M. B. Dobson. Temperature of air at great heights. *Roy. Soc., Proc.*, 103:339 – 341, 1923.

[3] H. Benndorf. Experimental exploration of upper atmosphere layers. *Phys. Zeits.*, 30:97 – 115, 1929.

[4] D. F. Martyn and O. O. Pulley. Temperature and constituents of the upper atmosphere. *Roy. Soc., Proc.*, 154A:455 – 486, 1936.

[5] L. Vegard. Terrestrial and solar coronæ and their relation to cosmic phenomena. *Gerlands Beitr. z. Geophys.*, 32:288 – 300, 1931.

[6] F. J. W. Whipple. Estimation of heights reached by airwaves which desend in zones of abnormal audibility. *Gerlands Beitr. z. Geophys.*, 31:158 – 168, 1931.

[7] E. H. Gowan. Effect of ozone on temperature of upper atmosphere. *Gerlands Beitr. z. Geophys.*, 24:57 – 59, 1929.

[8] F. L. Wipple. Photographic meteor studies. i. *Proc. Amer. Phil. Soc.*, 79, 1938.

[9] F. L. Wipple. Meteors and the earth's atmosphere. *Rev. Mod. Phys*, 15:246 – 264, 1943.

[10] J. S. Greenhow. Systematic wind measurements at altitudes of 80 – 100 km using radio echoes. *Phil. Mag.*, 7:471 – 490, 1954.

[11] J. S. Greenhow and E. L. Neufeld. The height variation of uper atmosphere winds. *Phil. Mag.*, 8:1157 – 1171, 1956.

[12] S. H. Marsh. A winds doppler facility for AMOR. Master's thesis, University of Canterbury, 1996.

[13] G. Brasseur and S. Solomon. *Aeronomy of the Middle Atmosphere.* D. Reidel Publishing Company, Holland, 2 edition, 1986.

[14] R. R. Garcia and S. Solomon. Numerical model of the zonally averaged dynamical and chemical structure of the middle atmosphere. *J. Geophys. Res.*, 88:1379 – 1400, 1983.

[15] Yu. I. Portnyagin, J. M. Forbes, T. V. Solovjeva, S. Miyahara, and C. DeLuca. Momentum and heat sourse of the mesosphere and lower thermosphere regions 70 – 100 km. *J. Atmos. Terr. Phys.*, 57:967 – 977, 1995.

[16] Yu. I. Portnyagin and T. V. Solovjeva. The role of vertical momentum fluxes in maintaining global meridional circulation in the lower thermosphere/upper mesosphere. *J. Atmos. Terr. Phys.*, 59:511 – 525, 1997.

[17] L. G. H. Huxley. The persistence of meteor trails. *Aust. J. Sci. Res.*, 5:10 – 16, 1952.

[18] R. L. Closs, J. A. Clegg, and T. R. Kaiser. Experimental study of radio reflections from meteor trails. *Phil. Mag.*, 44(350), 1953.

[19] W. Jones. The decay of radar echoes from meteors with particular reference to their use in the determination of temperature fluctuations near the mesopause. *Annales Geophysicae - Atmospheres Hydrospheres and Space Sci.*, 13(10):1104 – 1106, 1995.

[20] H. Brysk. Electromagnetic scattering by low-density meteor trails. *J. Geophys. Res.*, 63:693 – 716, 1958.

[21] G. N. Watson. *Theory of Bessel Functions.* Cambridge University Press, New York, 1952. p. 393.

[22] D. W. R. McKinley. *Meteor science and engineering.* McGraw-Hill Book Company, Inc, New York, 1961.

[23] W. J. Baggaley and T. E. Webb. The thermalization of a meteoric plasma. *J. Atmos. Terr. Phys.*, 39:1399 – 1403, 1977.

[24] E. F. Howick. Atmospheric parameters from three station radio-meteor data. Master's thesis, University of Canterbury, 1991.

[25] J. S. Greenhow and E. L. Neufeld. The diffusion of ionized meteor trails in the upper atmosphere. *J. Atmos. Terr. Phys.*, 6:133 – 140, 1955.

[26] A. A. Weiss. Diffusion coefficients from the rate of decay of meteor trails. *Aust. J. Phys.*, 8:279 – 288, 1955.

[27] J. S. Greenhow and J. E. Hall. The height variation of the ambipolar diffusion coefficient for meteor trails. *Planet. Space Sci.*, 5:109 – 114, 1961.

[28] M. Tsutsumi, T. Tsuda, T. Nakamura, K. Kita, T. Uehara, S. Kato, and S. Fukao. Meteor wind observations with the MU radar. *Radio Sci.*, 26:857 – 869, 1991.

[29] M. Tsutsumi, T. Tsuda, T. Nakamura, and S. Fukao. Temperature fluctuations near the mesopause inferred from meteor observations with the middle and upper atmosphere radar. *Radio Sci.*, 29:599 – 610, 1994.

[30] M. Tsutsumi. *A study of atmospheric dynamics near the mesopause using radio meteor echoes.* PhD thesis, Kyoto University, 1995.

[31] M. Tsutsumi, T. Tsuda, T. Nakamura, and S. Fukao. Wind velocity and temperature fluctuations due to a 2-day wave observed with radio meteor echoes. *J. Geophys. Res.*, 101:9425 – 9432, 1996.

[32] H. W. Ellis, M. G. Thackston, E. W. McDaniel, and E. A. Mason. Transport properties of gaseous ions over a wide energy range, III. *At. Data Nucl. Data Tables*, 31, 1984.

[33] A. D. Taylor. *A Meteor Orbit Radar.* PhD thesis, University of Canterbury, 1991.

[34] W. J. Baggaley, R. G. T. Bennett, D. I. Steel, and A. D. Taylor. The advanced meteor orbit radar facility: AMOR. *Q. J. R. astr. Soc.*, 35:293 – 320, 1994.

[35] W. J. Baggaley and R. G. T. Bennett. The meteoriod orbit facility AMOR: Recent developments. In B. Å. S. Gustafson and M. S. Hanner, editors, *Physics, Chemistry and Dynamics of Interplanetary Dust*, volume 104 of *ASP Conference Series*, 1996.

[36] W. H. Press, B. P. Flannery, S. A. Teukolsky, and W T Vetterling. *Numerical Recipes in Pascal.* 1989, Cambridge University Press.

[37] W. Jones and J. Jones. Ionic diffusion in meteor trains. *J. Atmos. Terr. Phys.*, 52(3):185 – 191, 1990.

[38] F. Verniani. An analysis of the physical parameters of 5659 faint radio meteors. *J. Geophys. Res.*, 78(35):8429 – 8462, 1973.

[39] W. J. Baggaley. The analysis of meteor data. In I. Halliday and B. A. McIntosh, editors, *Solid particles in the Solar System.* IAU, 1980.

[40] C. E. Meek, I. M. Reid, and A. H. Manson. Observations of mesospheric wind velocities 1. gravity wave horizontal scales and phase velocities determined from spaced wind observations. *Radio Sci.*, 20:1363 – 1382, 1985.

[41] T. Tsuda, S. Kato, T. Yokoi, T. Inoue, M. Yamamoto, T. E. VanZandt, S. Fukao, and T. Sato. Gravity waves in the mesosphere observed with the middle and upper atmosphere radar. *Radio Sci.*, 26:1005 – 1018, 1990.

[42] A. H. Manson, C. E. Meek, H. Teitelbaum, F. Vial, R. Schminder, D. Kürschner, M. J. Smith, G. J. Fraser, and R. R. Clark. Climatologies of semi-diurnal and diurnal tides in the middle atmosphere (70 – 110 km) at middle latitudes (40 – 50°). *J. Atmos. Terr. Phys.*, 51:579 – 593, 1989.

[43] A. E. Hedin. Extension of the thermosphere model into the middle and lower atmosphere. *J. Geophys. Res.*, 96(A2):1159 – 1172, 1991.

[44] A. E. Hedin. Msis-86 thermospheric model. *J. Geophys. Res.*, 92:4649 – 4662, 1987.

[45] A. E. Hedin. A revised thermospheric model based on mass spectrometer and incoherent scatter data. *J. Geophys. Res.*, 88:10,170 – 10,188, 1983.

[46] J. Barnett and M. Corney. Middle atmosphere reference model derived from satellite data. In K. Labitzke, J. Barnett, and B. Edwards, editors, *Handb. MAP, 16.* Sci. Comm. for Sol.-Terr. Phys. Secr., Univ. of Ill., Urbana, 1985a.

[47] J. Jones. On the decay of underdense radio meteor echoes. *Mon. Not. R. astr. Soc.*, 173:637 – 647, 1975.